CHAPTER 9
LIDAR MEASUREMENTS

This chapter describes a collection of lidar measurements along a vertical path at the Nd:YAG laser 532-nm second-harmonic wavelength carried out with the system this work has contributed to design. They comprise both atmospheric structure studies (i.e. lidar sensing of the atmosphere up to the boundary layer extent at approximately 3 km) and cloud studies at different range intervals (up to 15-km height). Previously, careful attention is devoted to the optical overlap factor, which plays a noticeable effect on the measurements. Though both theoretical and practical investigation is presented, mechanical inaccuracies in both positioning angles of the telescope (azimuth and elevation) seriously limit a good quantitative assessment of the overlap factor effects on the inverted profiles.

Practical techniques and limitations concerning the inversion algorithms, such as the inversion by range slices and the first live-scene application of the Kalman filter, are also presented.

Detailed physical and meteorological interpretation of the measurements and validation of absolute extinction figures are beyond our scope except for some cross-correlation with some literature references, as it would require the help of other sensing systems, such as meteorological radars or balloon-borne probes.

1. OVERLAP FACTOR EFFECTS ON THE MEASUREMENTS

1.1 Overlap factor under the uniform approximation

The *overlap factor (ovf)* was introduced in Chap.3, Sect.1.2. There, it was shown that interpretation of short-range lidar measurements must take proper account of the geometrical factors involved. In Ap.2, the ovf function, $\xi(R)$, (eq.9 in Chap.3) is solved for its *singular points,* that is, the points where $\xi(R)$ has null or unity value.
In addition, expressions are given to compute the *asymptotic values* of $\xi(R)$ at very long ranges so as to enable proper interpretation of long-range measurements. With a view to help measurement campaigns, Ap.2 encloses tables of singular points for different combinations of laser divergence angle, telescope field-of-view and separations of the telescope and laser axes at the lidar. From these tables one can see that the minimum angular precision required is about *50 μrad.*

1.2 Bidimensional ovf and coplanar adjustment

In the biaxial arrangement of the lidar system of the UPC, however, the problem is further complicated by the fact that the telescope has an equatorial mounting that enables movements both in this angle, γ, and in elevation, θ. This leads to a bidimensional problem, where the effective overlap factor is defined as the product

$$\xi(\delta,R) = \xi(\theta,R)\,\xi(\gamma,R) \qquad (1)$$

where

$\xi(\delta,R)$ is the effective ovf in the inclination angle between the laser and telescope axes, δ,

$\xi(\theta,R)$ is the overlap factor in the elevation, θ and,

$\xi(\gamma,R)$ is the overlap factor in the equatorial angle, γ.

The large angular inaccuracies of the telescope in both γ and θ angles have made impossible accurate determination of the range interval where the overlap factor is unity. In both angles, the telescope can be moved by means of multiturn screws. By substitution of the ocular lens by a *1-inch calibrated screen* it was possible to assess the angular accuracy in elevation by measuring the differential displacement of the lidar received pattern in the screen (Fig.4). After 1 turn, *5-mm* displacement was measured in the screen. Considering the telescope has a focal length of *2 m,* this results in *2.5 mrad/turn.* Assuming that the manual precision is about an eighth of turn, the maximum angular precision turns out to be about *300 μrad,* which is six times higher than the required one. In the equatorial angle, the movements are still much more critic, the angular precision being about ten times worse.

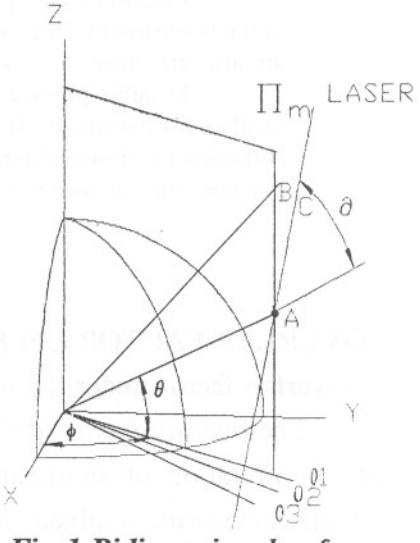

Fig.1 Bidimensional ovf.

By unscrewing the telescope mount, it was possible to move the telescope in the azimuth angle, ϕ. The three main angles, θ, ϕ and δ are represented in Fig.1, where the telescope is at the centre of coordinates. Note that the main problem of this biaxial arrangement is that the laser beam does not belong to the meridian plane Π_m, which is swept by successive movements in the elevation angle. Under this situation, the ovf is ruled by eq.(1). Provided angular accuracies good enough and the successive approximations algorithm sketched in Fig.2, it is possible to progressively tilt the plane Π_m so that the laser beam and the telescope axis become coplanar. Once this is achieved, the ovf problem reduces to a one-dimensional problem, as the one described in Chap.3, Sect.1.2.

The iterative algorithm is depicted in Fig.2. Abscissae and ordinates correspond to the equator and meridian projections, respectively. Consequently, the laser beam is tilted downwards. The procedure is a matter of cycling through these four steps (the letters in brackets indicate a point and a line in Fig.2, the latter of which indicates successive projections of the meridian):

- Turn the telescope mount to adjust ϕ and get maximum signal (A, r_o);
- move to a new elevation $\theta+\Delta\theta$ (B,r_o). At this point return-signal is lost;
- adjust γ to tilt the telescope until return-signal is recovered (C,r_1);
- return to the initial elevation θ (D,r_1) and so on (i.e. go to step 1 (A',r_2),...).

Despite the large angular inaccuracies of the mechanics, the algorithms was put into action to make the laser beam be as coplanar as possible to the meridian plane of the telescope. At the beginning, half a turn of the elevation screw was enough to loose track of the return-signal in the *1-in* projection screen while at the end, it was possible to keep track of the signal for eight complete turns *(≈ 40 mrad)*.

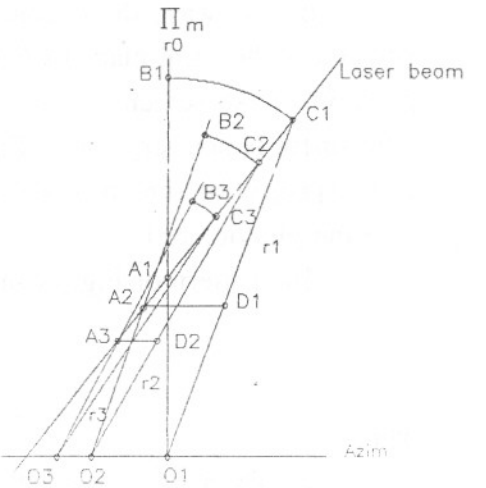

Fig.2 Adjustment procedure.

1.3 Interpretation of the lidar return-signal in the focal plane of the telescope

To our purposes, the telescope can be considered as a simple *(objective)* lens. The objective forms an image of a faraway object onto its focal plane. Following the notation and sign convention introduced in Fig.3, the objective forms a real, inverted image, approximately at the focal plane if the object is far enough. If the telescope were to be used for visual observation, an *ocular* or *magnififer* would aid the eye to examine this tiny real image. To detect the backscattered radiation, a photodetector will be placed instead on the focal plane.

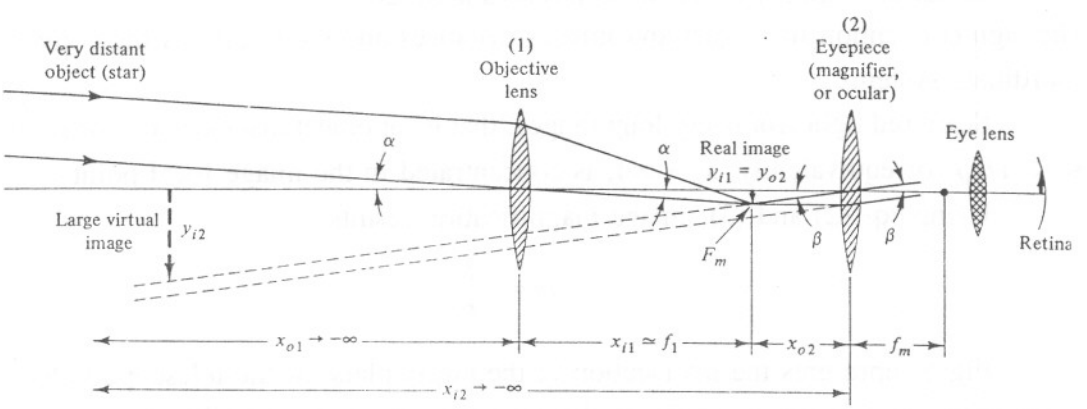

Fig.3 Optical diagram of a simple telescope.

The lidar telescope is a *Celestron C-8 telescope* with a Schmidt-Cassegrain configuration, 20-cm aperture diameter and 2-m focal length. In addition, it includes a revolver ocular holder facility where the ocular, or other elements can be assembled. In the present case, the ocular can be replaced by either the lidar receiver or an *1-inch* millimetred projection screen. The centre of the screen approximately coincides with the position of the APD when the revolver is turned to direct light onto its surface.

In this way, the eyepiece has been replaced by the projection screen, which is situated at the focal plane of the telescope *($x=f_1$)*. By means of a micrometric screw, the position of the screen in the focal plane of the telescope can be adjusted, though this adjustment is not very critic. Fig.4 shows the real image of the lidar return-signal on the *1-inch* projection screen (slight aberration is due to the use of powerful close-up lenses to take the photograph).

The pattern of Fig.4 can be interpreted by considering the *thin-lens equation* [26]

$$-\frac{1}{x_o}+\frac{1}{x_i}=\frac{1}{f} \tag{2}$$

where

x_o is the object distance to the thin-lens,
x_i is the image distance to the thin-lens and,
f is the focal length of the thin-lens *($f=2$ m)*.

and the *magnification m* [26] can be expressed as

$$m=\frac{y_i}{y_o}=\frac{x_i}{x_o} \tag{3}$$

where

y_o is object size,
y_i is the image size and,
the rest of variables have already been defined in eq.(2).

The sign convention for object and images distances and sizes follows the convention of coordinate systems.

Scattered light from very long ranges, that is, at object distances $x_o=-R$ so that *($1/R << 1/x_i$)* (or equivalently, $x_o \rightarrow -\infty$), is concentrated in the image focal point $x_i=f$.

Using eqs.(2) and (3), image magnification results

$$m=-\frac{f}{R} \tag{4}$$

Fig.5 represents the intersection in the target plane of the telescope field-of-view circle with the *1/e* power circle of the gaussian beam at range R. The radius of the telescope field-of-view, $r_T(R)$ and the radius of the laser in the target plane, $W(R)$, are given by eq.(10) and eq.(11) of *Sect.1.2 of Chap.3,* respectively.

Far away enough from the telescope, light scattered from the target plane *($x_o=-R$)* has an object size

$$y_o(R)=\pm W(R)+d(R) \tag{5}$$

From eq.(4) and Fig.5, the image size in the focal plane can be computed as

$$y_i=-\frac{f}{R}[\pm W(R)+d(R)] \tag{6}$$

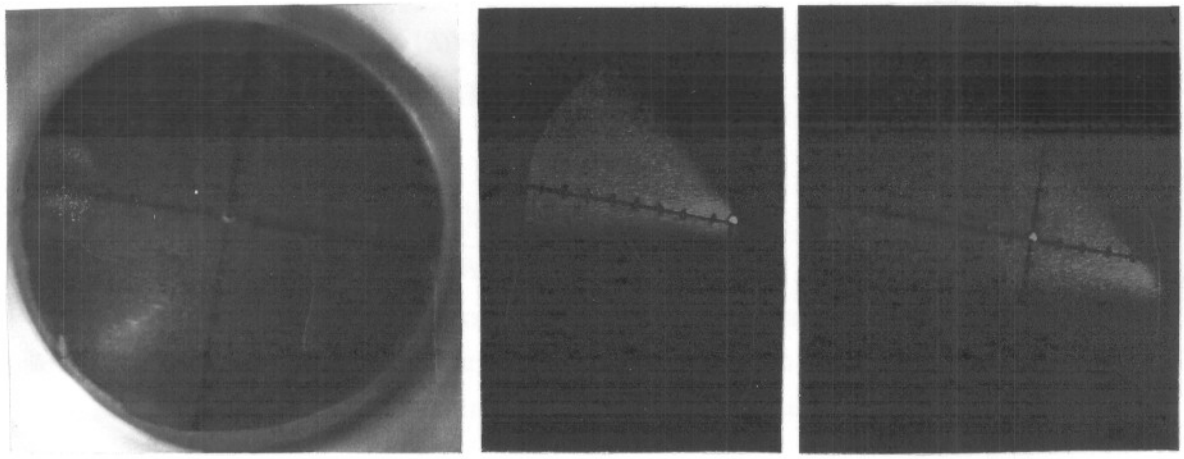

Fig.4 Image of the lidar signal on the focal plane of the telescope for three elevations: a) 1 turn left ($\Delta\theta \approx$ -5 mrad), b) centred ($\Delta\theta \approx 0$ mrad), c) 1 turn right ($\Delta\theta \approx +5$ mrad).

Substitution of eqs.(10),(11) and (12) of Chap.3 back into eq.(6), yields

$$y_i = -\frac{f}{R}\left[\pm\sqrt{W_o^2 + \theta^2 R^2} + d_o - \delta R\right] \tag{7}$$

where

$$\theta = \frac{\lambda}{\pi W_0} \tag{8}$$

Eq.(7) can be approximated for far- and near-field situations of the laser beam. Using eq.(8) above and eq.(11) from Chap.3, the far-field condition can be expressed as $R >> \lambda/\pi\theta^2$. Assuming $\theta = 0.1$ mrad, **one can conclude that laser beam is fully in the far-field for $R \approx 200$ m.**

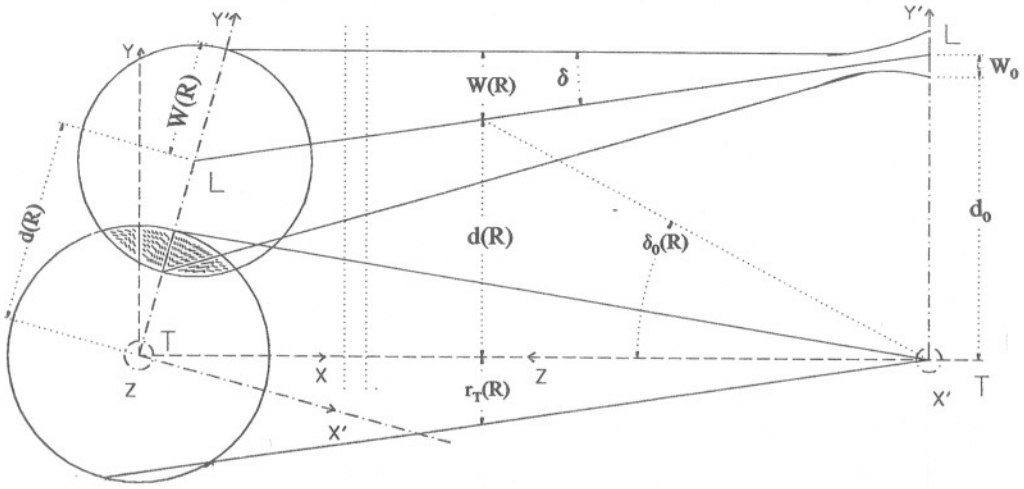

Fig.5 Intersection at range R of the gaussian spot power circle at 1/e (L) with the field-of-view of the telescope (T) showing the overlap area and related variables.

In the far-field of the laser beam radius $W(R) \approx \theta R$ and eq.(7) takes the form

$$y_i = -f[\pm\theta] - f[\Omega(R) - \delta] \tag{9}$$

where

$$\Omega(R) = \frac{d_o}{R} \tag{10}$$

The square brackets of eq.(9) evidence two important terms:

The first one of the right member let us understand *the telescope as an angle-to-position transducer.* Thus, any ray emerging from a distant circle $W(R)$ reaches the focal plane at a position:

$$\Delta y_i = -f\Delta\theta \tag{11}$$

where $\Delta\theta$ is the angle between the ray path and the telescope axis. As a result, *laser beam circles in the far-range are imaged as circles of constant size in the pattern of Fig.4, provided they are far enough.*

The second term of the right member represents a shift in position which, in turn, is formed by a constant shift due to the inclination angle between the laser and telescope axes, δ, and a range-dependent shift, $-f\Omega(R)$. At very far ranges, this term may become negligible compared to δ. Letting apart this range-dependent shift, the effect of different constant shifts because of movements in elevation is clearly evidenced in Fig.4. Fig.4b corresponds to the case where the laser and telescope axes are virtually parallel $(\delta=0)$, so that very far returns are imaged as an small spot of dimensions $\pm f\theta$ centred around the centre of the mask or, more precisely, around $-f\Omega(R)$ for closer positions still belonging to the far-field of the laser beam.

Under near-field conditions $(W(R) \approx W_0)$ the beam radius can be considered constant with range and eq.(7) becomes

$$y_i = -\frac{f}{R}[\pm W_o] - f[\Omega(R) - \delta] \tag{12}$$

Again, the second term of the right member shows the shift in position due to $\Omega(R)$ and δ, but now, the behaviour of the first member is substantially different. The laser beam circles of the near-field are imaged as patterns whose size is larger and larger as long as the circles are closer and closer to the telescope. In addition, as the range becomes shorter, their image becomes blurred as it no longer forms in the focal plane. This is clearly shown in Fig.4: Points belonging to the contour of the triangle-shaped pattern of Fig.4c are points not far enough from the telescope while the round spot formed at the apex of the pattern corresponds to the far-field laser beam circle image (except perhaps by the term $-f\Omega(R)$ that tends to move the far field circles to some inner position in the pattern). Finally, the case of Fig.4a corresponds to $\delta<0$ (telescope slightly aimed in opposite direction to the laser).

Alternatively, similar results can be retrieved by following a matrix ray formulation to the problem [26].

1.4 Inclusion of the Gaussian spot behaviour

The most concerning points about the effects of the ovf on the lidar measurements are the inclusion of the Gaussian behaviour and the search of simple methods to solve the bidimensional problem formulated in eq.(1) and sketched in Fig.5. The bidimensional problem can always be reduced to a one-dimensional problem by a turn in coordinates as indicated in Fig.5. A practical procedure to perform this turn of coordinates has been described in Sect.1.2.

If misfocusing effects are disregarded, the overlap factor problem of Fig.5 can be translated into the focal plane of the telescope by considering the range-dependent radius of the laser beam image in the focal plane rather than in the target plane. If the spot is assumed to be gaussian with radius $r_s(R)$ at $1/\sqrt{e}$ field intensity and the detector radius is r_D, it is easy matter to compute the power fraction falling onto when the spot is miscentred by a distance $\rho_0(R)$ as

$$\xi(R) = \frac{1}{r_s(R)^2} e^{-\frac{\rho_0(R)}{2r_s(R)^2}} \int_0^{R_D} e^{-\frac{\rho^2}{2r_s(R)^2}} I_0\left(\frac{\rho_0(R)\,\rho}{r_s(R)^2}\right)\rho\, d\rho \qquad (13)$$

where $I_o(x)$ is the modified Bessel function of zero order and first kind [6].

Now, let us compute the related variables as follows:

By noting from Sect.1.3 that a telescope can be understood as an angle-to-position transducer with gain $-f$, $\rho_{0(R)}$ can be computed as the focal length times the angular size of the separation $d(R)$ between the telescope and laser axes seen on the telescope (Fig.5).

$$\rho_0(R) = -f\delta_0(R) \; ; \qquad \delta_0(R) = -\frac{d(R)}{R} \qquad (14)$$

Likewise, the gaussian spot radius on the focal plane can be computed as

$$r_s(R) = \frac{f}{\sqrt{2}}\frac{W(R)}{R} \qquad (15)$$

where the factor $1/\sqrt{2}$ compensates the definition of $W(R)$ at $1/e$ field intensity rather than at $1/\sqrt{e}$ [25].

Fig.6 plots the overlap factor based on eq.(13) for the same three uniform situations studied in Fig.4, Chap.3. Comparing both figures and the tables of Ap.2, the gaussian behaviour yields much slower slopes than the uniform case. Thus, for instance, an inclination of $\delta = 0$ *mrad,* yields *1800-m* rising distance *(10%-90%)* where the range-return lidar signal is falsified.

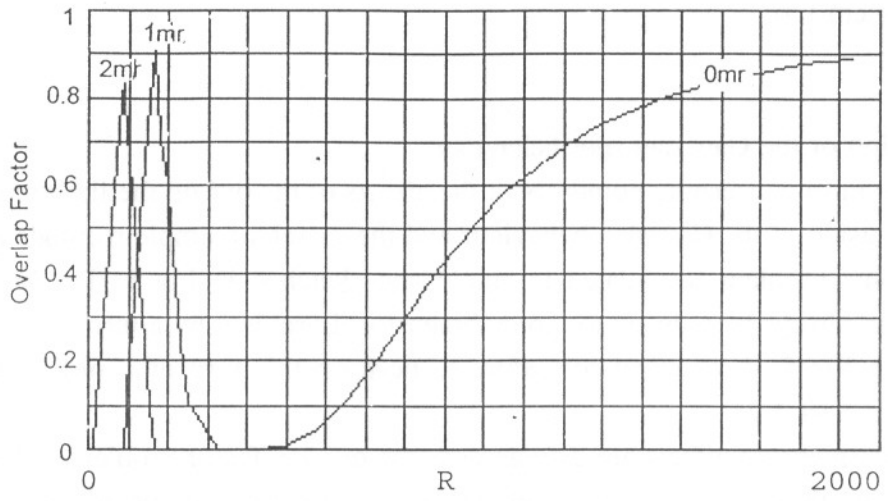

Fig.6 Gaussian overlap factor $\xi(R)$ (d_o=18 cm and δ=0, 1 and 2 mrad).

1.5 Effect of the overlap factor on the measurements

1.5.1 Practical considerations

Unfortunately, even though analytical methods and practical procedures have been derived in the preceding sections to study the effect of the ovf on the measurements, telescope mechanical imprecisions are too large to enable quantitative discussion.

The core of the lidar measurement campaign has consisted in ceilometry studies (cloud height extent), which usually lie between *500 m* and *6 km,* and structure observation (pollution monitoring) up to *3 km. For each experiment, different overlap range intervals had to be adjusted accordingly.* The following procedure was followed:

First and as a rule of thumb, the apex of the triangle-shaped pattern was situated as close as possible to the centre of the *1-inch* projection screen in the focal plane of the telescope. After that, *θ and γ angles were as finely adjusted as the mechanical precision allowed to enhance the signal strength read-out in the oscilloscope along the range interval of interest.* In spite of the fact that the telescope lacks precise angular scales, relative angular movements can be monitored reasonably well by reading the net displacement of the apex on the millimetred screen and counting turns of the multiturn elevation screw. For instance, if the displacement readout were Δy_i, the angular variation in δ would be

$$\Delta\delta = \frac{\Delta y_i[mm]}{f[m]} \qquad [mrad] \tag{16}$$

Ovf adjustments for different elevation angles δ, during the structure measurement campaign are shown in Fig.7 to Fig.12. In Fig.7, where the apex is at the centre-left of the screen, the telescope and laser axes were made slightly divergent, so that the return-signal from the structure range interval was very faint. Little by little, the inclination angle δ was adjusted so as to move the apex towards the centre of the screen. As a result, the

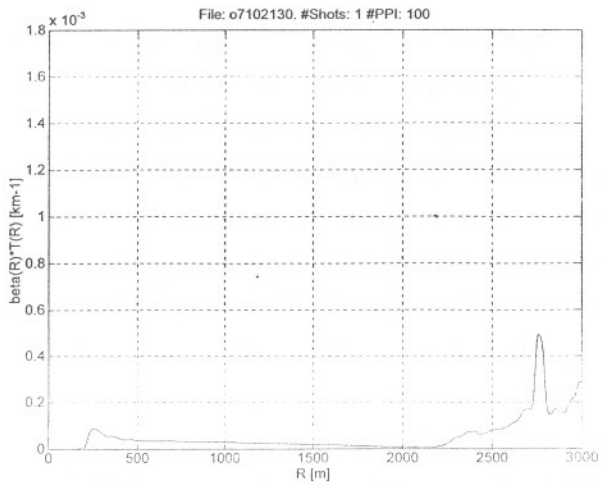

Fig.7 Structure (apex centre-left).

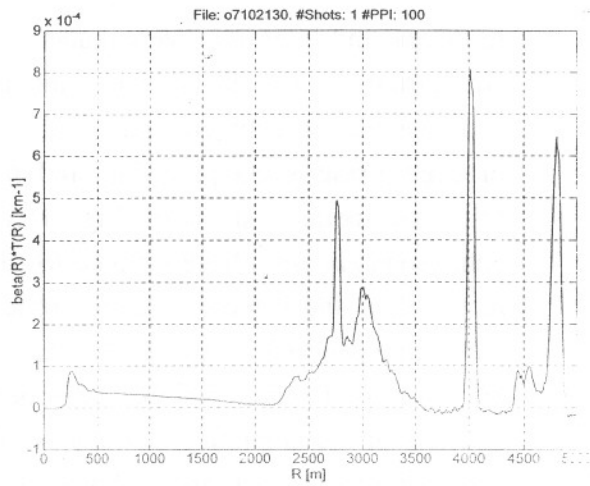

Fig.8 5-km profile (apex centre-left).

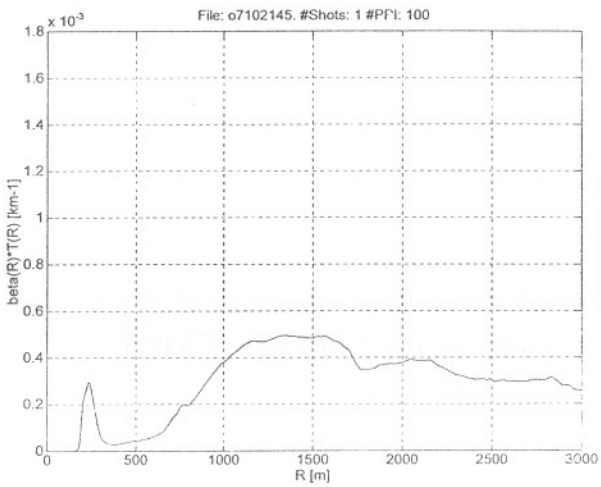

Fig.9 Structure (apex centre).

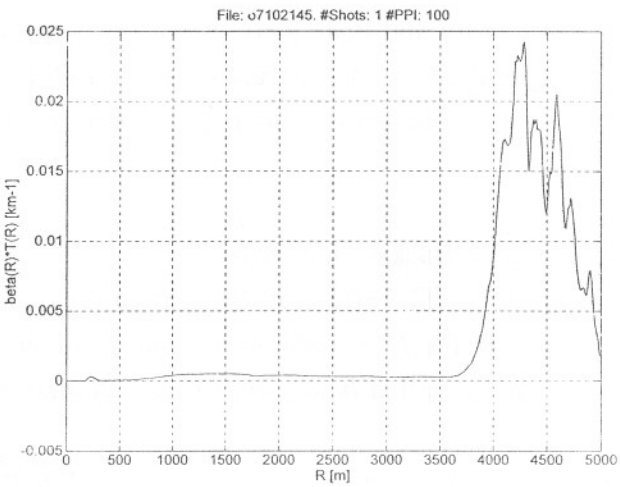

Fig.10 5-km profile (apex centre).

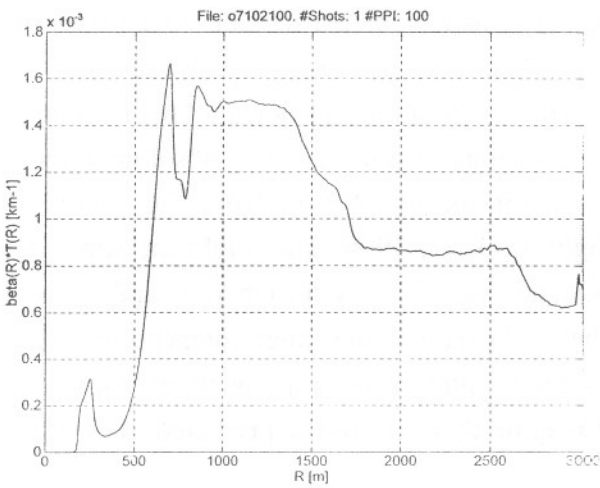

Fig.11 Structure (apex centre+azimuth).

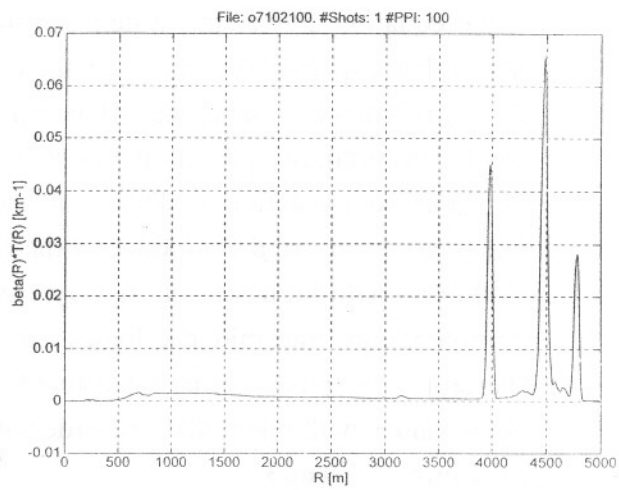

Fig.12 5-km profile (apex centre+azimuth).

NOTE: The figures above represent three pairs of R^2-corrected profiles. Pairs are formed by 3-km and 5-km range-interval profiles. The notation +azimuth *indicates an adjustment in azimuth.*

telescope and laser axes were made virtually parallel. In Fig.9, the return-signal from the structure up to *3 km* has grown in intensity. At this end position adjustment was very critic and one had to rely on range-corrected information from the control unit monitor to proceed further in the procedure and manage to maximize the signal-strength by extremely fine movements in azimuth. Fig.11 corresponds to the same situation as Fig.9 but with enhanced azimuth. (Note from eq.(9) that the laser beam far-field begins approximately at $R > 200\ m$ and it tends to concentrate very close to the apex. Moreover $\Omega(R)$ decreases with increasing range and hence, the spot position is no longer offset). Clouds about 3-4 km are a good help to end the adjustment quite confidently since they can be used as signal markers of the beginning of the unwanted range-interval (see Fig.8, Fig.10 and Fig.12). Since slight trimming of the elevation θ, led to significant changes in the amplitude of the detected clouds, it may well be guessed that the inclination angle had to be between *0 and 1 mrad* and that, therefore, a fast slope could result. This latter assumption may well be justified by the appearance of an initial bump around *200 m*.

Basically, this is the procedure followed before any lidar measurement is made.

1.5.2 Backscatter errors

The effect of the overlap factor *(ovf)* on the lidar inversion can be easily inferred from the R^2*-corrected* fashion of the *single-scattering lidar equation* (Chap.7. eq.(1)) or the so-called *backscatter-transmittance product* (β*-T product)*.

$$\beta T(R) \doteq \frac{R^2 P(R)}{A} = \beta(R) \exp\left[-2 \int_0^R \alpha(r)\, dr\right] \tag{17}$$

In the equation above, the system constant A (Chap.7 eq.(2)) includes ovf losses. This means that any underestimation of the ovf $\xi(R)$ in the flat range (i.e between $R_{min}^{(2)}$ and $R_{max}^{(2)}$) results in the same misestimation for the backscatter-coefficient. This is to say that angular uncertainties prevent the inversion algorithms from retrieving absolute values for the backscatter-coefficient. This is also shown in the set of plots from Fig.7 to Fig.12, which represent the β*-T* product on the night of Oct.7, 1996. That night the atmospheric condition could be described as *very clear* (see Figs.5 and 6 in Chap.3) and, as a first approximation, transmittance losses can be neglected for the range interval up to *3 km*. Therefore, the plots can be interpreted as backscatter plots. Among them, only Fig.11 yields values within less that one order of magnitude lower to the predicted ones in Fig.5 and Fig.6 of Chap.3.

Conversely, since the extinction is always retrieved in nonmemory algorithms by differential methods that cancel out system constant uncertainties, it is still possible to retrieve absolute figures of this parameter on the condition that the ovf is constant over the range-selected interval (Sect.1.5.1).

2. PRACTICAL ASPECTS AND LIMITATIONS OF THE INVERSION ALGORITHMS

2.1 Inversion by slices

It has often been assumed that since the atmosphere is more likely to be homogeneous over small rather than large intervals, by applying the inversion algorithms available to a succession of small intervals, a reasonable inversion of the sought-after parameters, extinction and backscatter, may also be achieved [186].

The following subsections discuss this point for the inversion algorithms developed in the preceding chapters (Chaps.7 and 8).

The procedure is illustrated over the range-corrected lidar profile of Fig.13 to Fig.16, where successive application of slope-method and least-squares algorithms have been performed for each subsection over the 15-km profile. This is also known as the *slice-method.* Application of hybrid Klett's method to a 10-km interval using the backward solution form of Sect.4.1, Chap.7 is superimposed in the same figure.

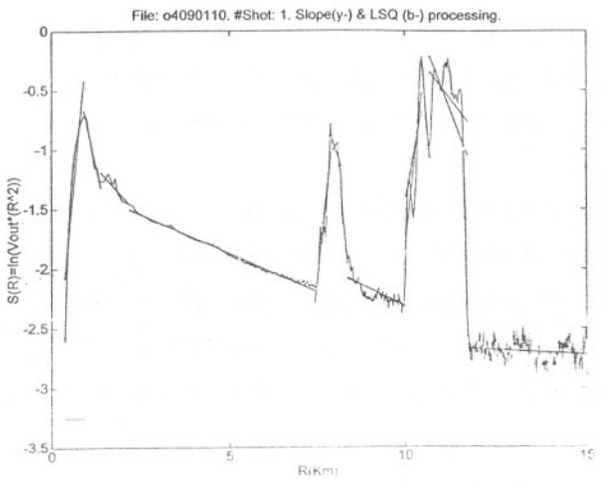

Fig.13 15-km profile showing slices.

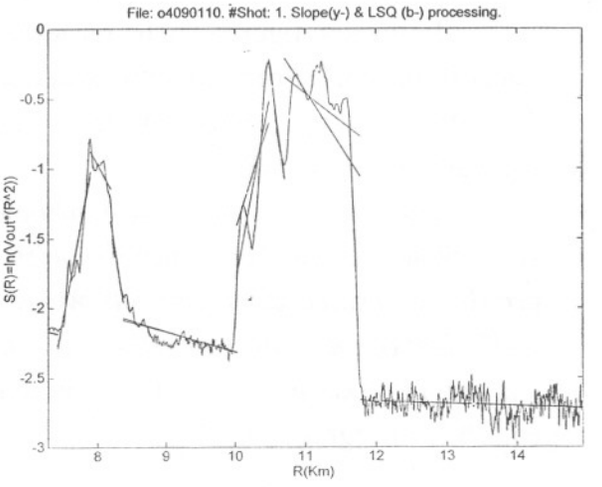

Fig.14 Upper part of the 15-km profile.

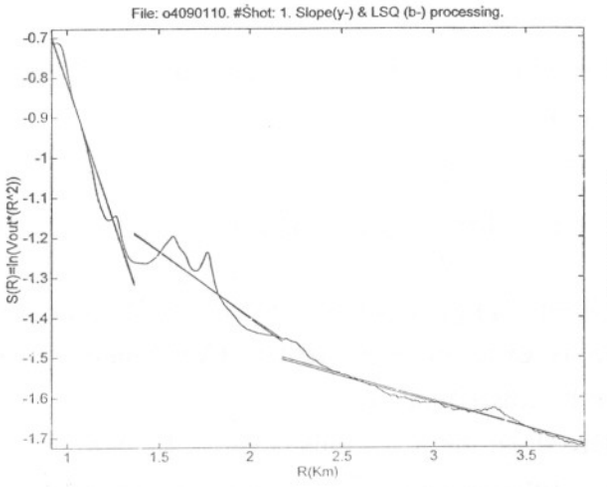

Fig.15 Lower range-interval (detail A).

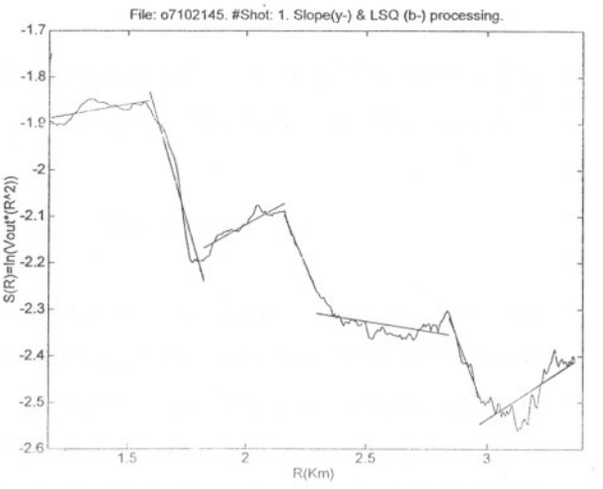

Fig.16 Lower range-interval (detail B).

2.1.1 Application of Slope-Method and Least-Squares algorithms

The differential equation corresponding to the single-scattering lidar equation in terms of the range corrected function, *S(R)*, (eq.(28), Chap.7) can be written as

$$\frac{dS(R)}{dR} = \frac{1}{\beta(R)}\frac{d\beta(R)}{dR} - 2\alpha(R) \tag{18}$$

From this equation, it is clear that the application of slope-method and least-squares algorithms over small intervals leads to the conjecture that

$$\frac{1}{\beta(R)}\left|\frac{d\beta(R)}{dR}\right| \ll 2\alpha(R) \tag{19}$$

at least over most of the* S(R) *curve. Unfortunately, assumptions like this are not well justified for many situations of interest, e.g. under the conditions prevailing in dense clouds (Fig.14), smoke or *in any situation where significant local inhomogeneities occur.*

Extinction figures can be retrieved fairly accurately in all the homogeneous range-intervals of Fig.13, perhaps with exception of some inner intervals in clouds where eq.(19) fails due to large extinction peaks that cause important fluctuations in $d\alpha/dR$ or equivalently, in $d\beta/dR$.

The impact of such local inhomogeneities is much worse for the backscatter-coefficient than for the extinction-coefficient. ***A priori, when homogeneous slices of the profile are preceded by intervals where large inhomogeneities occur, the backscatter-coefficient can no longer be estimated.*** This is the case of the range-intervals *(8.2-9.8) km* and *(11.7-15) km* in Fig.14. The affirmation above can be better understood by rewriting eq.(18) in integral form

$$S(R) = \ln[A\,\beta(R)] - 2\int_0^R \alpha(r)\,dr \tag{20}$$

and assuming that the first homogeneous interval begins at $R > R_1$. Then, for $R > R_1$, and defining $\alpha=\alpha(R_1)$, eq.(20) can be expressed as

$$S(R) = \left[\ln[A\,\beta(R)] - 2\int_0^{R_1} [\alpha(r) - \alpha_1]\,dr\right] - 2\alpha R \qquad R > R_1 \tag{21}$$

By linear regression analysis it is found that eq.(21) provides an intercept at $R=0$ that is equal to the term into brackets rather than to the expected term, $ln(A\beta)$. Consequently, the inverted backscatter-coefficient turns out to be misestimated.

A posteriori, the range-intervals where slope-method yields negative figures for the extinction-coefficient (positive slopes in the set Fig.13 to Fig.16) turn out to be good estimates of the excess-area represented by the integral term in eq.(21), even though such extinction figures bear no physical significance at all.

The same conclusions apply to the least-squares case, since it is a close variant to the former method with exception of the kind of regression fitting.

2.1.2 Choosing Klett's parameters

The most concerning points about the automation of Klett's method are the inputs of a suitable calibration α_m (eq.28, Chap.7) and correlation constant k (eq.27, Chap.7).

To solve the former point, the automatic implementation of the algorithm resorts to the very simple least-squares estimate of α_m over the homogeneous slice selected by the user, or the nearest one where homogenous nonmemory-type algorithms can be applied. It must be noted, however that such estimate of α_m will not be very accurate for atmospheres of high visibility, particularly if large fractional changes in extinction occur (this is also illustrated by the error plots given of Chap.7, Sect.3.3.2). In such cases, extra information, for example from balloon-borne measurements, would be highly valuable to improve the inversion.

As for the correlation constant, k, the software developed combines the backward solution exposed in Chap.7 Sect.4.1 eq.(31),

$$\frac{dS(R)}{dR} = \frac{k}{\alpha}\frac{d\alpha(R)}{dR} - 2\alpha(R) \tag{22}$$

with multi-objective norm minimization of eq.(29), Chap.7, at different slices where the slope of the range-corrected function can be estimated fairly well. Formally,

$$\min_k \left\| slope(R_i) - \frac{d\hat{S}(R_i,k)}{dR} \right\|^2 ; \qquad i = 1..N \tag{23}$$

where

$slope(R_i)$ is the calibration in slope at point R_i,

$S(R)$ is the range corrected function estimation for correlation k and,

R_i are the mesh of points where norm-minimization applies.

Note that for each step of the norm-minimization procedure, the extinction profile must be recalculated.

Since k depends on the lidar wavelength and various properties of the obscuring aerosol there is also room for user-entry corrections. As demonstrated earlier in Chap.7, Sect.4.2.2, eq.(22) does not strongly depend on the choice of k, provided $k \in (0.67, 1)$. The expertise gained through inversion of real data confirms 1 as the most common value for the inversion of structures and soft profiles, where $k \approx 0.7$ is often used for clouds.

The extent of agreement of all the inversions performed is as good as it should be expected, leaving just the uncertainties associated with experimental data and the error plots of Chap.7 for the correlation constant k and the calibration α_m.

The only source of error which has not been considered before in the inversion procedures is the initial increase in the lidar signal shown in Fig.13, which is due to

incomplete overlap of the transmitter and receiver field-of-view during the first hundred meters. Yet, Klett's method implementation in link-detect can cope extremely well with this situation thanks to the backward integration procedure. Any misfit at the boundary end point (R_m) carry on through the length of interval to the initial hump but not vice versa.

2.2 Choosing the right PPI and IP parameters from the control unit

PPI (pulses per integration) and *IP (integrated packets)* parameters must be chosen according to the kind of atmospheric lidar study.

Regarding ceilometry studies (could height-time extent) and the very large signal-returns, not many integrations are necessary *(typ. PPI=5)* but long-time data records are needed *(typ. IP>50)* to perform real-time cloud monitoring. Conversely, in instances of pollution structure monitoring, the return-signal is very faint, and very large integration times are necessary. In Fig.13, where data is recorded up to 15-km height, a thousand integrations per packet were made. Typically, for ranges $<$ *3km,* typical values are *PPI=100, IP=1.*

2.3 Kalman filter practical considerations

In Chap.8 the Kalman filter was presented as an attractive algorithm that could theoretically supersede nonmemory algorithms in two respects: first, and for comparison to the Klett's method, the Kalman filter can be interpreted as the application of Klett's algorithm to successive range-intervals every time smaller and, in the limit, which were formed by a couple of samples. This situation corresponds to the real situation where the correlation constant, k, is also function of the range R. Hints to this kind range-dependent correlation are found in [186]. In the case of the undersampling filter of Chap.8, Sect.3, this is to say that both extinction- and backscatter-profiles can be inverted. Second, it was suggested that the Kalman filter could enhance inversion results by taking advantage of past-retrieved profiles.

For the time being, a practical Kalman filter has been developed based on a parallel processing version of the undersampling filter of Chap.8, Sect.3, and the additional simplification that linear correlation is assumed between α and β state-vector components

$$\vec{\alpha} = C\vec{\beta} \tag{24}$$

As a result, the state-vector can be written as

$$x \equiv \left[C \;\; \beta_1 \;\; \beta_2 \;\; \cdots \;\; \beta_{N/2}\right]^T \tag{25}$$

Note that this is equivalent to assume $\rho'=1$ (in-cell correlation) and $\rho=0$ (cell-to-cell correlation). *With these hypothesis the Kalman filter works very much like the Klett's method but now including memory and parallel processing features.*

The inversion of real data having practical signal-to-noise ratios (SNR) and an underlying physical model that cannot completely be known (the atmosphere), has revealed some important points concerning the Kalman filter. These are discussed next.

2.3.1 Physical model uncertainties and tracking capacity

Physical model uncertainties are basically caused by the hypothesis that $k=1$ and $C(R)=C$ in eq.(24), despite the fact that the correlation constant C is adaptive.

When the filter converges, this always leads to over or underestimation of the backscatter very much as it was described in Chap.8, Sect.3.5. Yet, for the purpose of retrieving backscatter colourmaps (Fig.19), only relative values are of interest.

The tracking capacity of the Kalman filter is extremely sensitive to the state-vector initialization and the state-noise covariance matrix Q_k is particularly critic. State-vector initialization relies in Montecarlo trials from the tabulated extinction and backscatter sets of Chap.7, Tab.4. The assumption of a good constant value for all the initial state-vector components (for instance, the mean value) is enough to start the filter successfully. Once the best initialization is identified, the filter is restarted but lowering Q_k. In fact, this would not strictly be necessary provided very long records of data were available. This is done, however, to force fast convergence of the filter making the most of the limited time-length of recorded data (usually 40 to 60 packets, or equivalently 1-Mb data). Conversely if Q_k is too high, the filter would invest too much time in reaching a reasonable solution. The invested time usually exceeds the recorded time-length and very often it leads to broad divergence of the filter array for higher variances in Q_k. It must be noted that since all the Kalman filters in the array work as cooperative entities, divergence of one single filter implies divergence of the whole set.

Very good results have come from cloud inversions, where very high SNRs enable steady-state behaviour virtually from the beginning. Moreover, if the Kalman filter is initialized via a Klett inversion, steady-state behaviour is assured from t_0. This is clearly shown in Fig.17 to Fig.20, where abscissae and ordinates represent the time and height axes, respectively. The axes ranges are *40 packets* in abscissae and between *3* and *5.5 km* approximately, in ordinates. By comparing the contour plots of Fig.18 with Fig.20, the powerful memory feature of the Kalman filter yields fairly confident results. This is clearly evidenced by the time continuity of the contour lines in Fig.20 which indicate progressive and soft modification of the contour based on past information. The effect is still more evident in the time interval where no clouds are detected. Whereas Klett's colourmap shows a sharp contrast between clouds (red-yellow) and clear-sky areas (blue), Kalman filter image does not. In Klett's contour counterpart, this is represented by a nearly vertical yellow contour line that defines a sharp boundary between both areas, which is far from any physical meaning.

Irrespective of how parallel processing arises, it must also take into account the situation dictated by the physical model. This is to say, that if the physical situation comprises a cloud layer at some height, each filter of the array must have enough observable samples from the layer to perform a successful inversion.

The parallel architecture is systolic. This means that for each iteration all the filters demultiplex observables, process data independently from each other and finally, multiplex state vectors in order to built the actual profile. The ripple level of the multiplexed solution is an indicator of the degree of accommodation of the same physical model by all the filters. Because of the independent processing, each filter *sees* different decimated samples from the same range interval and, for this reason, it is very important to ensure that all these observable samples belong to the same physical situation (cloud, fog, structure...).

2.3.2 Parameter observability

In Chap.8, Sect.5, it emerged that the extinction is a very low observability parameter, specially in situations of high visibility. A new outcome is that ***the first observation cell at R_{min} plays a dominant role in scaling the rest of the extinction and backscatter profiles.*** This can easily be corroborated by inspection of the observation matrix H_k (Chap.8, Sect.3.3, eq.(57)). In other words, assuming and undersampling factor $M=2$ (inversion on alternate cells), examination of the two-way path transmittance for $R_j > R_{min}$ yields

$$T(R_j) = \exp\left[-2\int_0^{R_j}\alpha(r)\,dr\right] = \exp\left\{-2\left[\alpha_1(R_{\min}+\Delta R)+\sum_{i=2}^{j/2}\alpha_i\cdot 2\,\Delta R\right]\right\} \tag{26}$$

where j is an even number.

The prominent role of the first sample can also be explained from eq.(26) above, where the first sample is weighted by a factor $R_{min}+\Delta R \approx R_{min}$ and the subsequent ones by a factor ΔR. The observability ratio for the first cell can be defined as

$$\mu = \frac{R_{\min}}{\Delta R} \tag{27}$$

Furthermore, estimation of this first sample α is still more concerning. For clarity reasons, let us consider a rectangle approximation for the transmittance integral of eq.(26). Doing so, assumes homogeneity for the atmospheric extinction α over the first interval $(0, R_{min})$, which is particularly doubtful considering that it is precisely within this first interval where the optical overlap factor may substantially mould the range-return power. Note that if the first sample is misestimated, the rest of the state-vector variables must compensate for the accumulated error over $[0,R_{min}]$.

2.3.3 State-noise covariance matrix assessment

The state-noise covariance matrix, Q_k, is without any shade of doubt, the most difficult parameter of the Kalman filter to assess. This is so, because it directly model the intrinsic behaviour of the atmosphere dynamics. In the case of vertical exploration with the lidar, this represent an extra difficulty to the algorithm, mainly because the assumption of a Gauss-Markov atmosphere are not valid any more because spatial correlation in the simplified way depicted by the graph of Fig.6, Chap.8 is only true inside of a layer of reduced extent, especially for horizontal exploration.

Many approaches were tried for Q_k. Some of them are the following:

- *Boosting Q_k:*

  This approach consists in deliberately increasing Q_k, as a way of telling the filter that the atmosphere has a large variance and that, consequently, the filter must open its search span to enable tracking. This is a good alternative during the Montecarlo initialization of the filter, which uses a boosted Q_k for a set of filter with different initializations. The ones that converge are restarted with a smaller Q_k. It must also be noted that convergence with large Q_k leads to poor solutions that are within the error-state space of solutions given the actual SNR. However, large values of Q_k always lead to divergence. As a rule of thumb, the first *5-to-10* steps during the trajectory search of the filter are very important; otherwise, since linearization is performed on the trajectory estimates rather than on the true trajectory (which is unknown), the filter is doomed to fail.

- *Frosting Q_k:*

  This second approach consists in reducing Q_k once the filter is in track-mode, usually by means of an scaling factor λ

  $$Q_{k+1} = \lambda Q_k \tag{28}$$

  In cloudy scenes, this method is of disadvantage, since this scenes always involve a large dynamism.

- *Diagonal and tridiagonal Q_k:*

  This are useful conventional formulations to Q_0 but believing that Kalman filter strength comes from its self-learning possibilities, a final and successful proposal for Q_k was reached as follows

- *Windowed Q_k:*

  For the time being, this is the best way of assessing Q_k letting apart diagonal or tridiagonal formulation for Q_0. It is based on successive computation of the state-vector covariance (basically, the inverted profiles). Thus at time t_k, the covariance is computed from k past realizations. The results obtained with this configuration are by far the best (see Fig.67 and Fig.68).

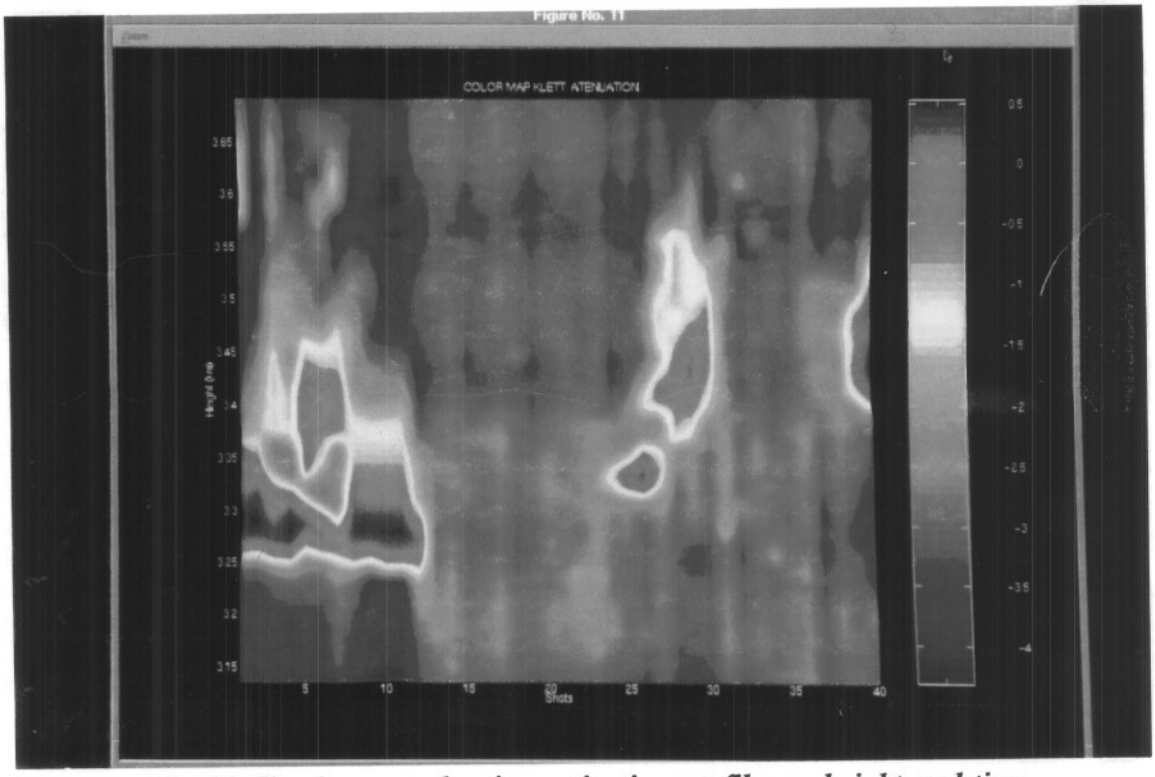

Fig.17 Cloudy scene showing extinction profile vs. height and time. (Relative scale colourmap using Hybrid Klett processing).

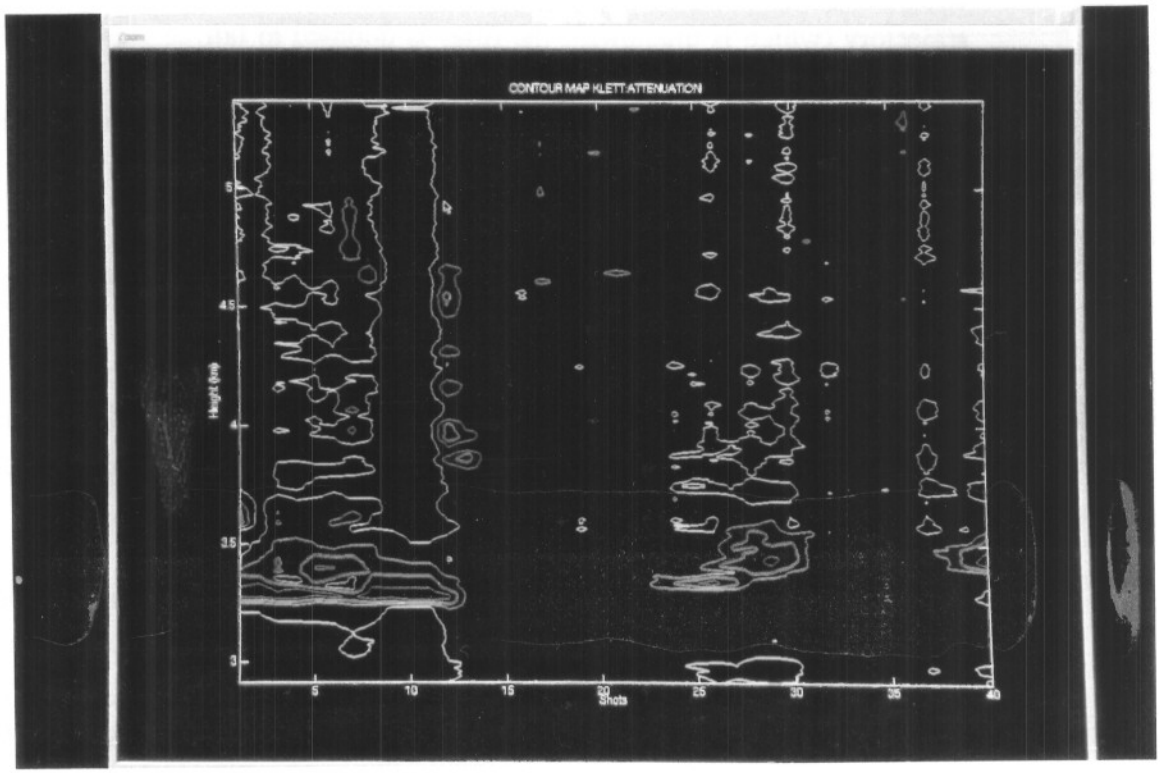

Fig.18 Iso-extinction contour lines for the cloudy scene above. (Relative scale contourmap using Hybrid Klett processing).

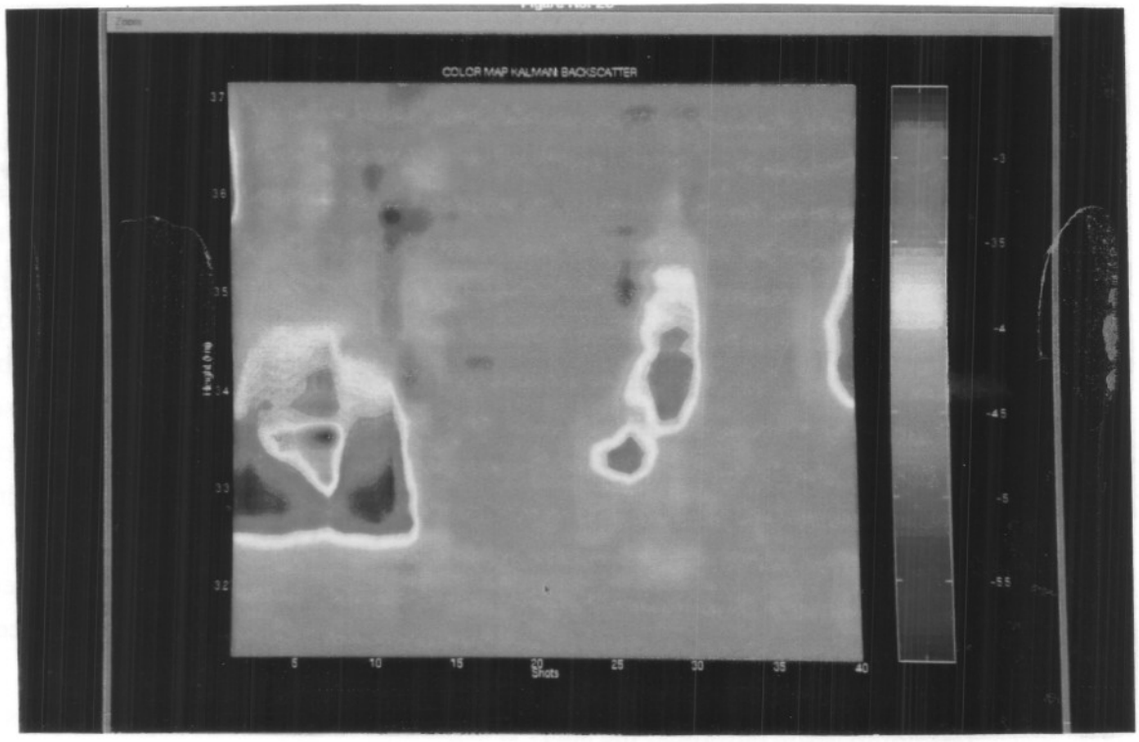

Fig.19 Cloudy scene showing extinction profile vs. height and time. (Relative scale colourmap using parallel Kalman processing).

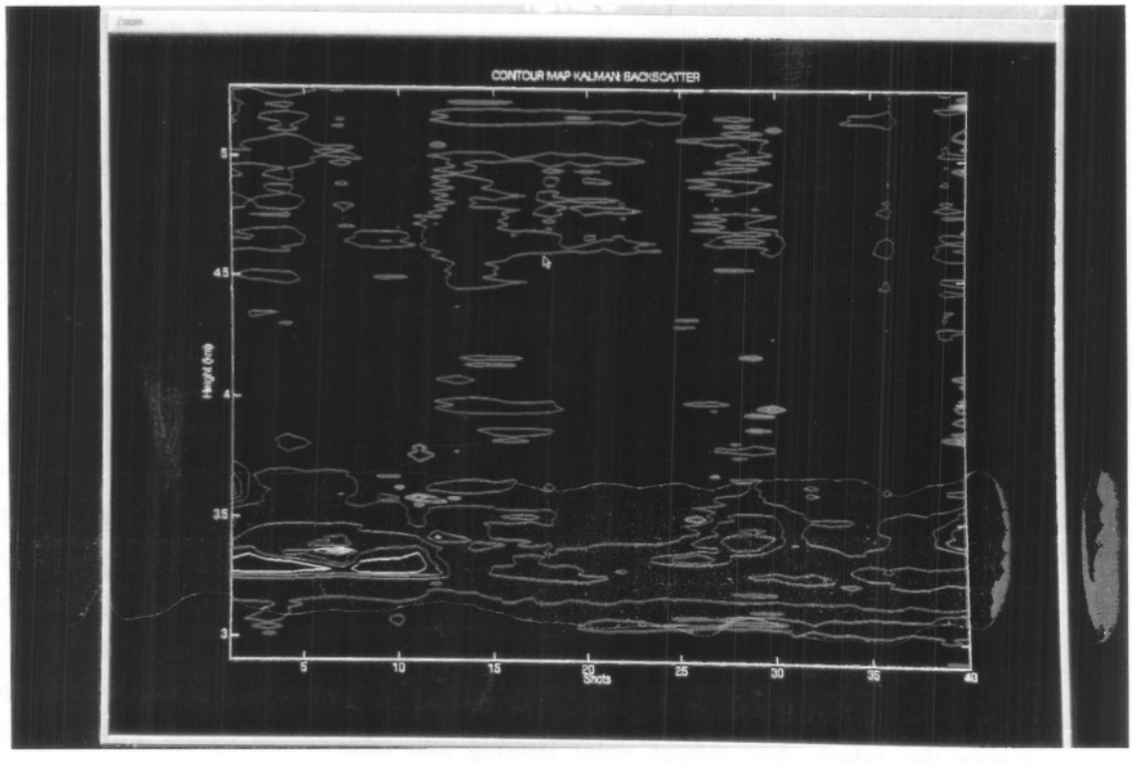

Fig.20 Iso-extinction contour lines for the cloudy scene above. (Relative scale contourmap using parallel Kalman processing).

3. ATMOSPHERIC STRUCTURE STUDIES

3.1 Day- and night-time observations in visually *clear* air

The suspended particles present in relatively clear air may be detected by the lidar technique. Such particles may reveal the *depth of the mixed layer* at the earth's surface or show the vertical extent, in the present case, of urban haze layers from which the presence of inversion layer may be inferred. Although the observations presented offer a unique method of evaluating atmospheric turbidity remotely, the most spectacular capability is in revealing features and structures (up to *3 km)* of the clear atmosphere. Examples showing recent measurements of such structure undertaken by the UPC lidar are illustrated by the four set of intensity plots comprising Fig.21 to Fig.26 (set 1), Fig.27 to Fig.32 (set 2), Fig.33 to Fig.38 (set 3) and Fig.39 to Fig.44 (set 4). They represent the *backscatter-transmittance product* (eq.(17)) for day- and night-time observations up to *3 km* during the 23 and 25 September 1996. Apart from its importance in public health, the *turbidity* of the polluted atmosphere is of significance in determining the transfer of radiant energy between the Sun, the Earth and the outer space. The differenc *radiant energy exchange* between day and night is clearly evidenced between sets 1 and 3.

For comparison purposes, the study is organized in two different pairs of sets. Day-time structure monitoring corresponds to sets 1 and 2 where the same plots are presented in fixed full scale (set 1) or autoscaled for each figure (set 2). The same organization applies for the night-time sets. (Detailed information is given as footnotes). The fixed scale for day-time plots is $1.2x10^{-3}$ $[km^{-1}]$ while for night-time plots is $2.5x10^{-4}$ *[km-1].*

By comparing successive time plots between *10:41 h* and *23:55 h (local time)* a successive decline in the range-return signal is observed. This trend is only broken by the plots at 18:35 h (Fig.35 or Fig.41) and at 23:55 h (Fig.38 or Fig.44). The reliability of such data sets as pollution measurements cannot be proved by the inherent miscalibration imposed by the overlap factor. The exact figures or even the approximate moulding of the profile by the overlap factor, if any, is for the moment a matter for conjecture. However, one may speculate that the possible moulding of the *β-T profiles* by the ovf can only be present during the first hundred meters, since the fast slope evidenced by the initial hump around this range, does not agree with the plots of Fig.6 for an optical adjustment nearby $\delta = 0$ *mrad.* Another feasible explanation that would be in favour of the strong ovf influence illustrated by Fig.6 *($\delta = 0$ mrad),* is that the initial bump ($1\text{-}5x10^{-5}$ km^{-1}) may correspond to large particulate pollutants returns or to a discontinuity at the boundary of an urban mixing layer ([25] p.352), both of which would be attenuated by the slow rising slope of the ovf curve up to around 1500 meters. This possibility seem less likely because there is no apparent reason to justify the virtual lack of signal between *200 and 400 m* during the whole day, where solar heating and convection cycles involve a changing dynamism in the layered structure. Note that at 18:35 h (Fig.35 or Fig.41) and 23:55 h (Fig.38 or Fig.44) some of this changes are evidenced.

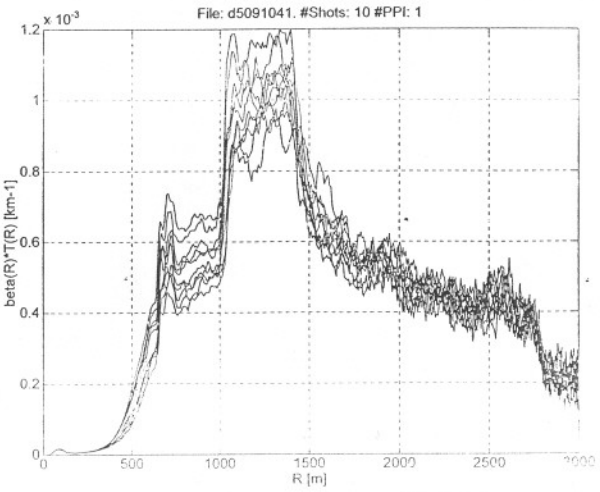

Fig.21 Sept. 25th at 10:41 h.

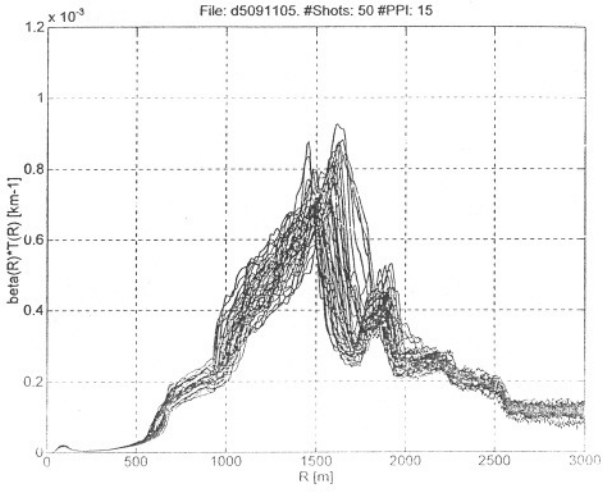

Fig.22 Sept. 25th at 11:05 h.

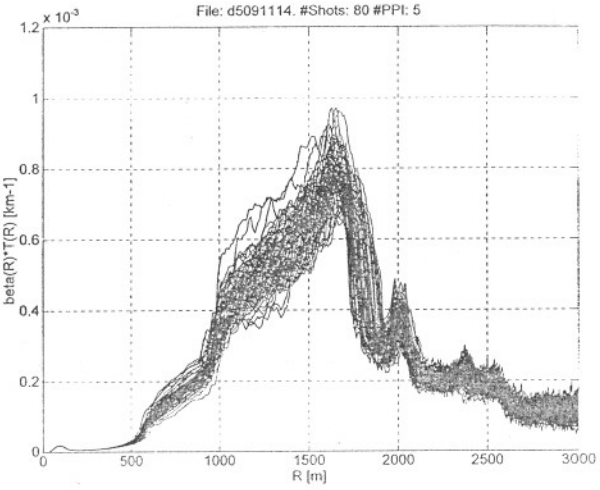

Fig.23 Sept. 25th at 11:14 h.

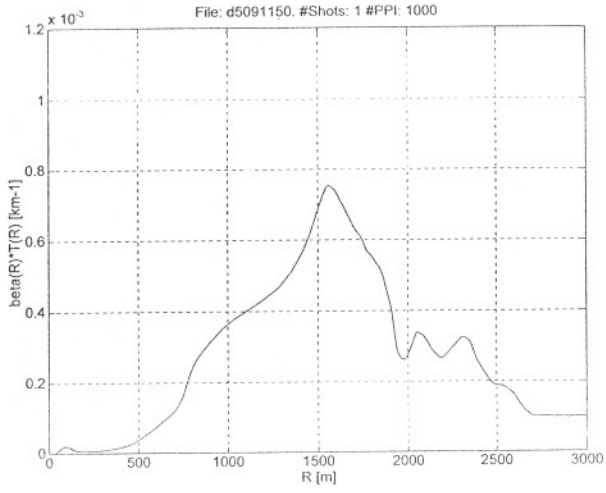

Fig.24 Sept. 25th at 11:50 h.

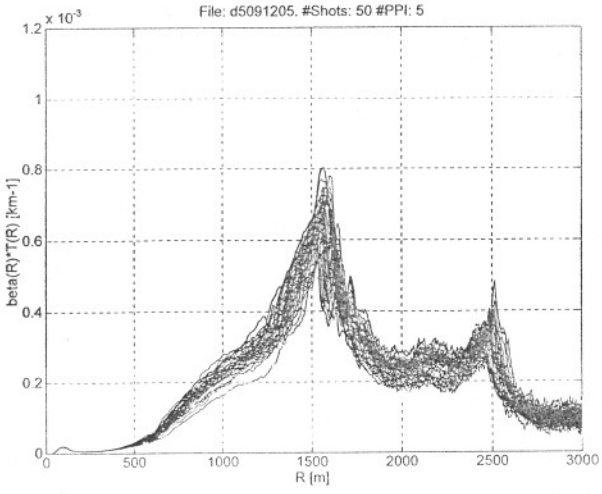

Fig.25 Sept. 25th at 12:05 h.

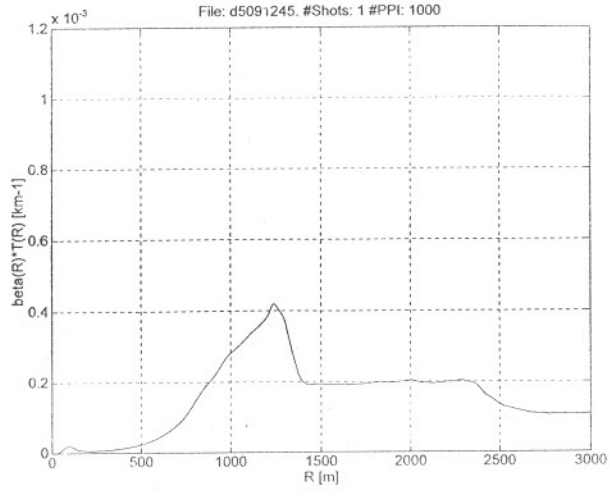

Fig.26 Sept. 25th at 12:45 h.

NOTE: Illustrations show day-time atmospheric evolution on Sept. 23rd and 25th, 1996 (fixed scale).

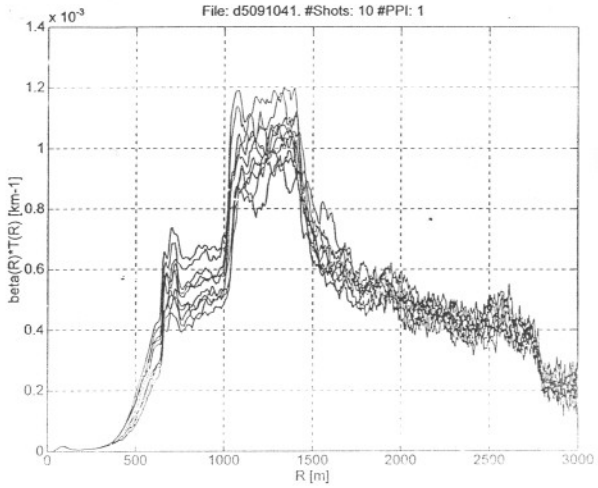

Fig.27 Sept. 25th at 10:41 h.

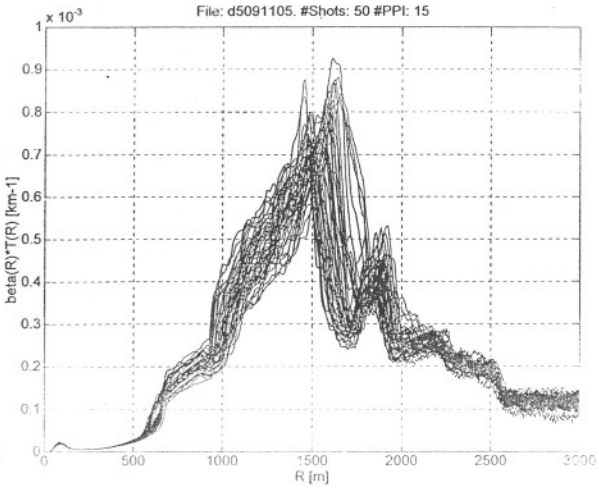

Fig.28 Sept. 25th at 11:05 h.

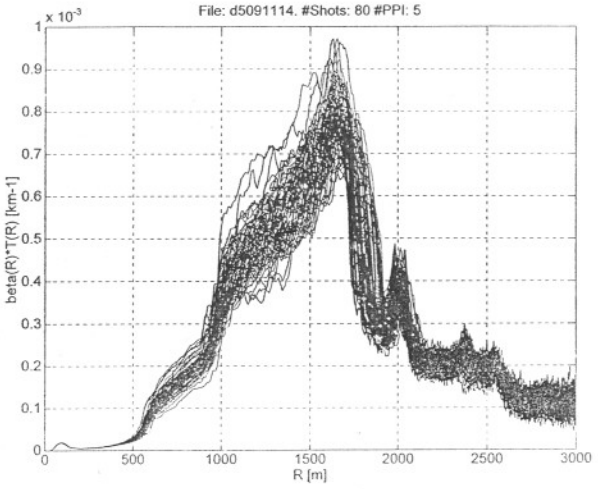

Fig.29 Sept. 25th at 11:14 h.

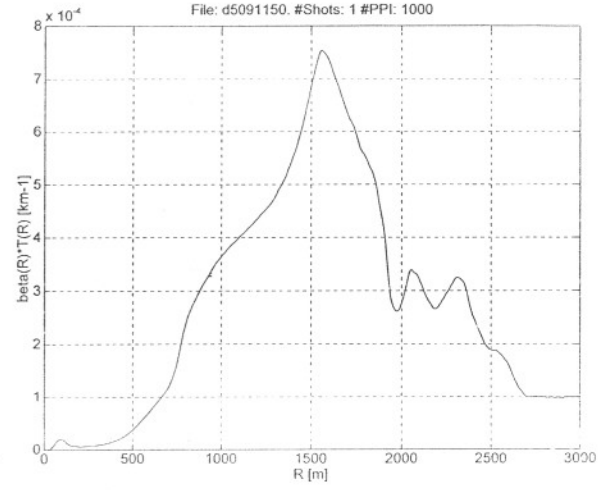

Fig.30 Sept. 25th at 11:50 h.

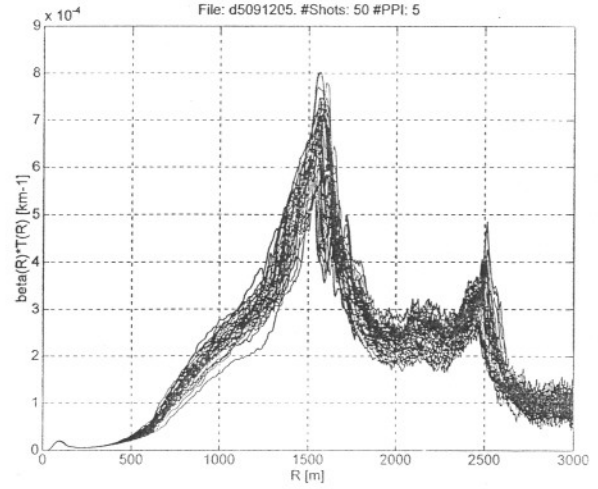

Fig.31 Sept. 25th at 12:05 h.

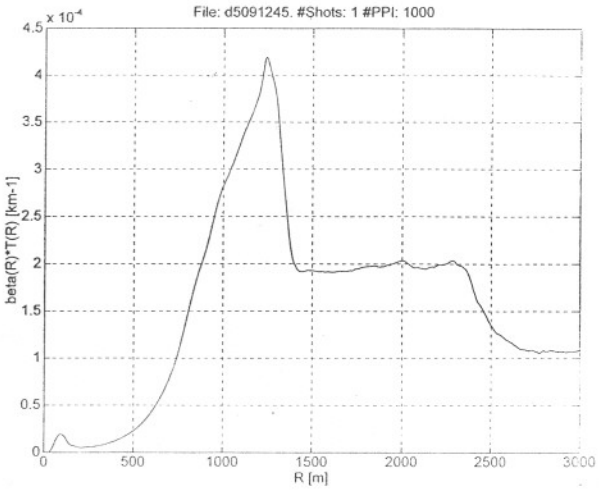

Fig.32 Sept. 25th at 12:45 h.

NOTE: Illustrations show day-time atmospheric evolution on Sept. 23rd and 25th, 1996 (autoscaled).

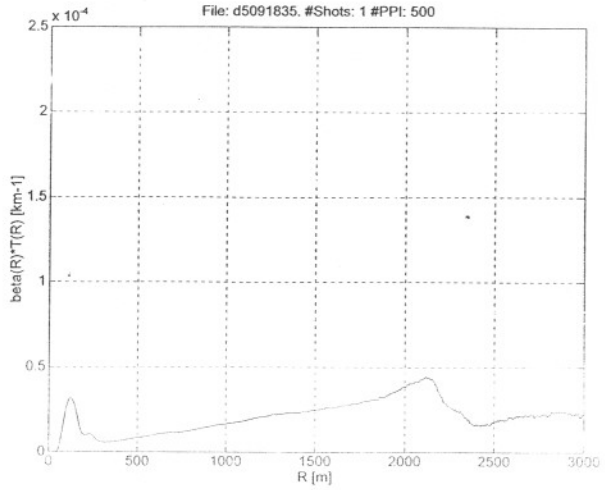

Fig.33 Sept. 25th at 18:35 h.

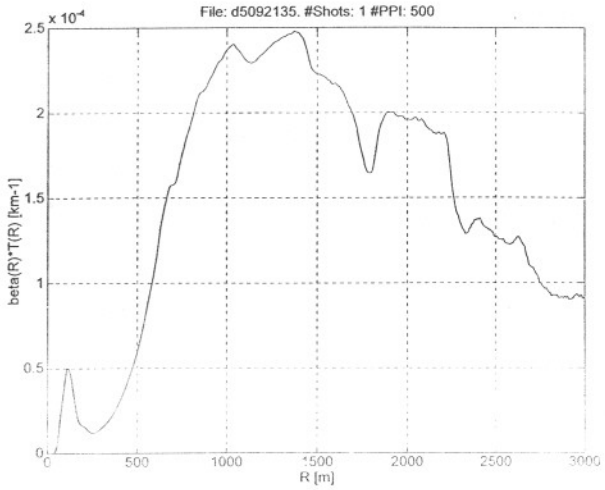

Fig.34 Sept. 25th at 21:35 h.

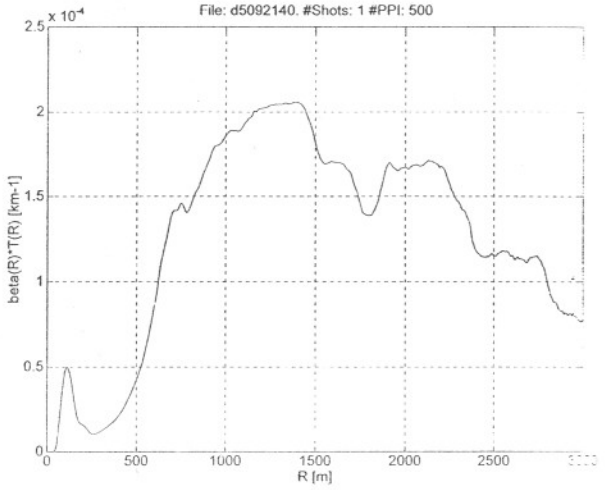

Fig.35 Sept. 25th at 21:40 h.

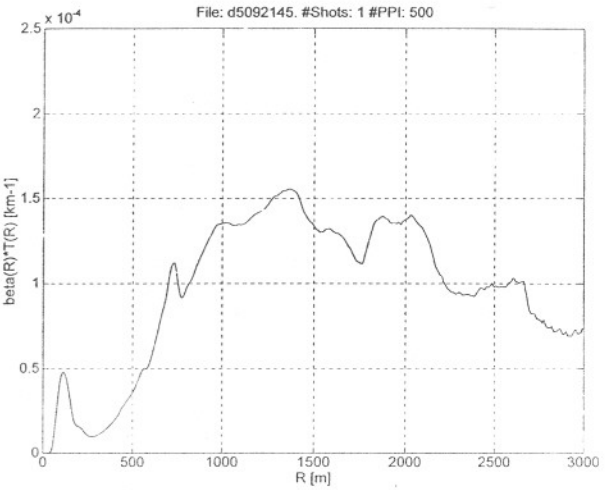

Fig.36 Sept. 25th at 21:45 h.

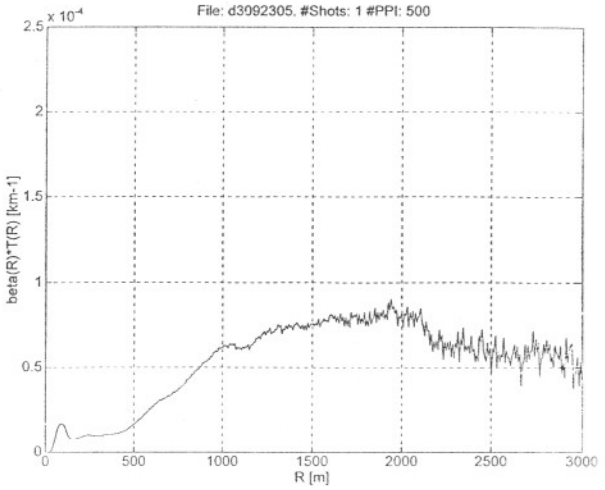

Fig.37 Sept. 23rd at 23:05 h.

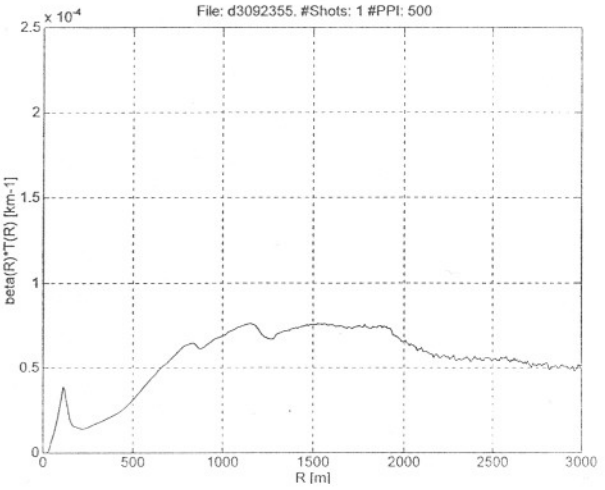

Fig.38 Sept. 23rd at 23:55 h.

NOTE: Illustrations show night-time atmospheric evolution on Sept. 23rd and 25 th, 1996 (fixed scale).

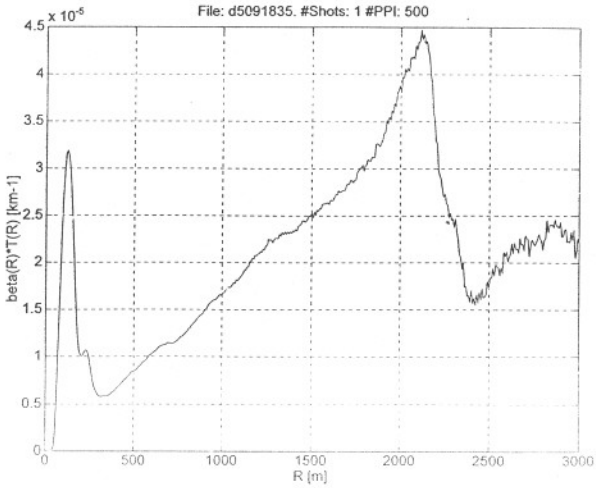

Fig.39 Sept. 25th at 18:35 h.

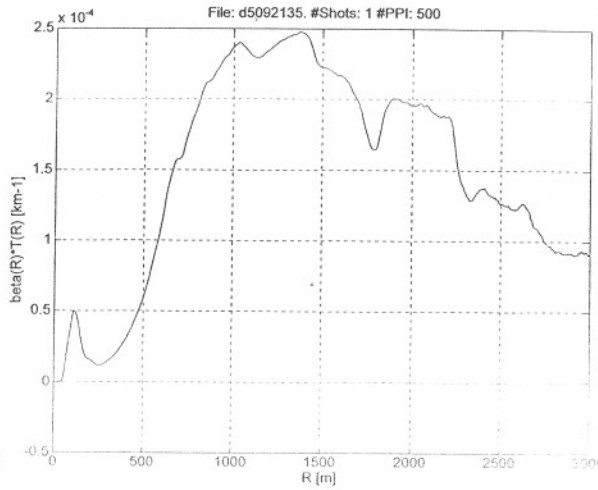

Fig.40 Sept. 25th at 21:35 h.

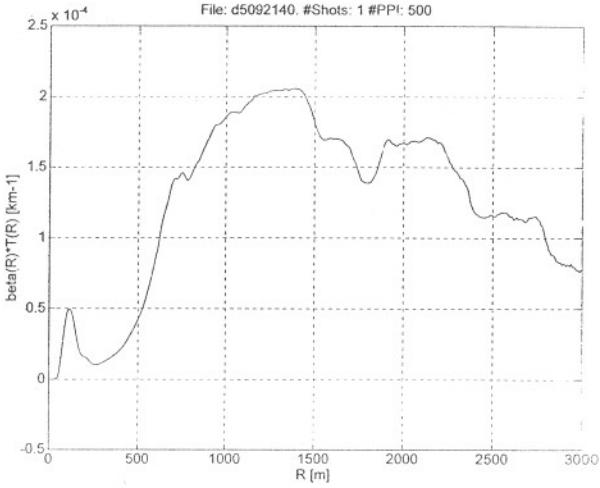

Fig.41 Sept. 25th at 21:40 h.

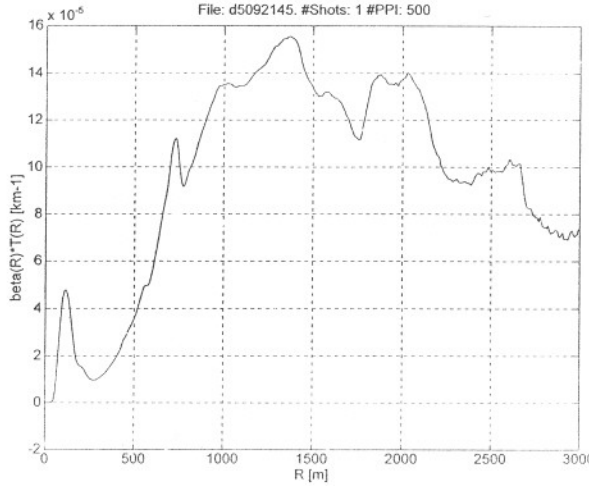

Fig.42 Sept. 25th at 21:45 h.

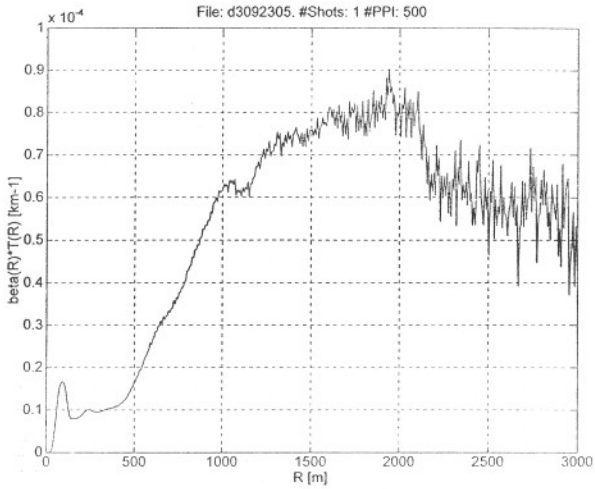

Fig.43 Sept. 23rd at 23:05 h.

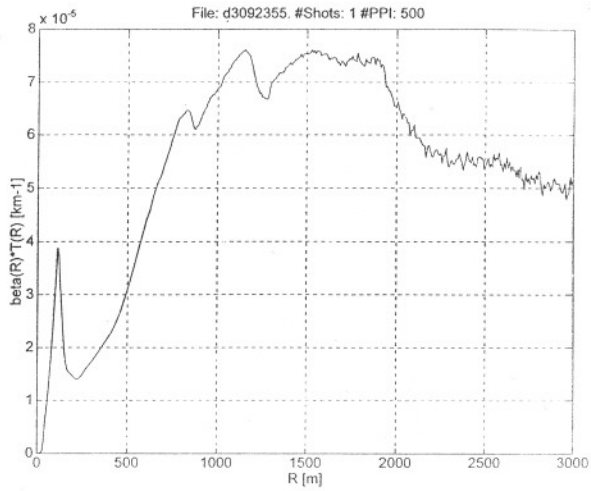

Fig.44 Sept. 23rd at 23:55 h.

NOTE: Illustrations show night-time atmospheric evolution on Sept. 23rd and 25 th, 1996 (autoscaled).

3.2 Retrieval of extinction and backscatter profiles

Fig.49 and Fig.50 plot Klett's extinction profiles for the day- and night-time situations of Fig.23 or Fig.29 and Fig.38 or Fig.44, respectively. According to Tab.1 and refs.[9][25], the situation at around noon (11:14 h) could be defined as *light haze* ($\alpha\epsilon$[0.4-0.9] km^{-1}) while at midnight (23:55 h) it could be defined as *standard clear* ($\alpha \approx 0.17 km^{-1}$). It must be warned that the mean extinctions, α_{inv}, shown in Tab.1 are computed in the interval *(1.5-3) km* rather than in the whole interval beginning at ground level. There are two reasons for that: the first one is that the extinction profile is quite homogeneous within the interval *1.5-3 km,* specially between *2-3 km.* (This is corroborated by slope method and least-squares inversions that yield similar extinction figures). The second reason is that by choosing such subinterval, the average value computed for the extinction is free from any possible ovf moulding effects. Perhaps, this is only true with the exception of a scaling factor due to the ovf but, since the extinction-coefficient inversion procedures are based on differential methods, such factor would play no role at all in the computed mean extinction figure. In addition, note in Fig.6 that the ovf stabilizes at approximately *2 km* for $\delta = 0$ *mrad.*

As for the backscatter profiles, they can easily be retrieved by substituting the following correlation constants back into eq.(27), Chap.7:

- **$C = 1.65 \times 10^{-3}$ (day-time)** - **$C = 6.67 \times 10^{-4}$ (night-time)** **(k=1)**

Since *k=1,* both extinction and backscatter profiles look exactly alike, except for a change in scale. By reference to Tab.1, ovf miscalibration is reencountered again as a mismatch between the expected and measured backscatter-coefficient, whose misestimation is above one order of magnitude the typical value expected from Tab.3, Chap.7.

Next, Fig.45 and Fig.46 illustrate linear time-height colour and contour diagrams, respectively, of the extinction-coefficient for the day-time situation at nearly noon (11:14h) of Fig.23 or Fig.29). The same colourplot of Fig.45 is reproduced again in Fig.47 using logarithmic scale and a different colourmap to enhance low structure areas (up to *1 km*). The colourbar on the right of the diagram indicates *absolute values* for the extinction-coefficient. Fig.48 summarizes both inverted extinction and backscatter-coefficients.

With regard to the inversion errors, they can only be tried to be assessed in the interval between *1.5-3 km* for the ovf reasons previously explained. According to the errorplots of Chap.7, Sect.4.2.3, the main error source in Klett's method comes from the

INVERSION			ATMOSPHERIC CONDITION based on refs.[9] [25]			
Time	α_{inv}	β_{inv}	α_{typ} [km^{-1}]	β_{typ} [km^{-1}]	V_M [km]	condition
11:14 h	$6 \cdot 10^{-1}$	$9.9 \cdot 10^{-4}$	$5 \cdot 10^{-1}$	$5\text{-}25 \cdot 10^{-3}$	8	light haze
23:55 h	$1.4 \cdot 10^{-1}$	$9.3 \cdot 10^{-5}$	$1.7 \cdot 10^{-1}$	$1.7\text{-}8.5 \cdot 10^{-3}$	23.5	standard clear

Tab.1 Comparison between structure optical parameters inverted and referenced.

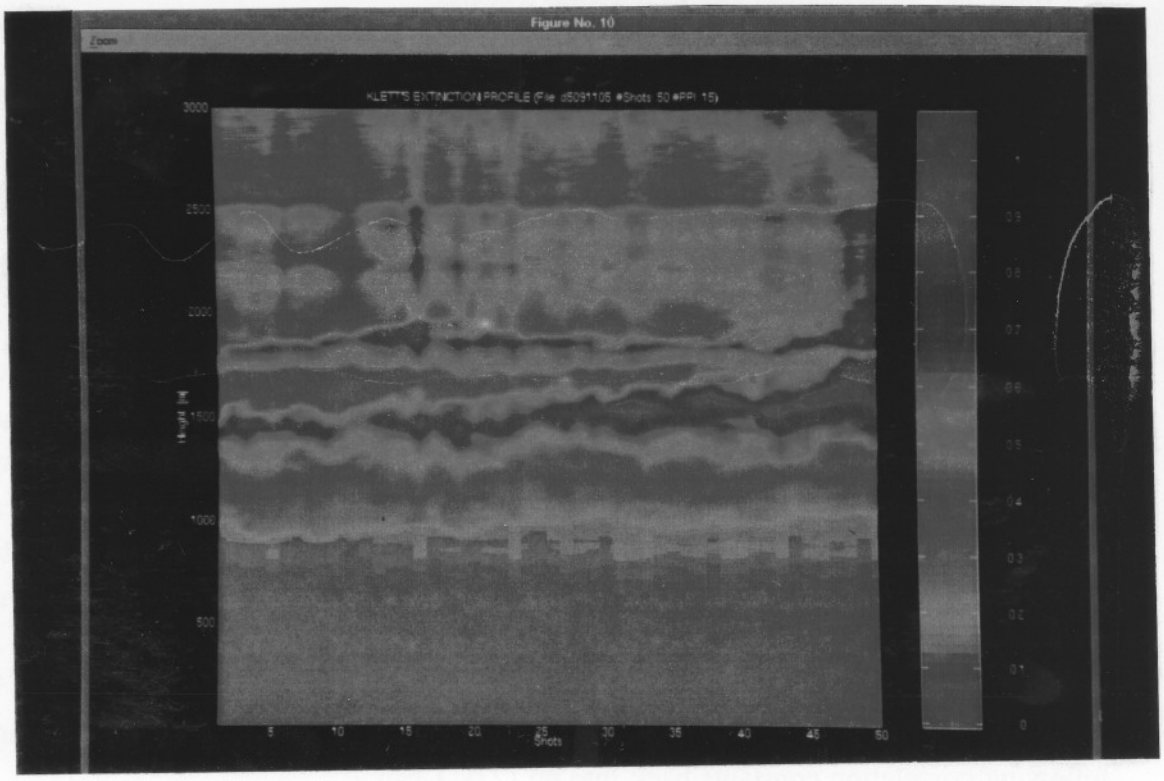

Fig. 45 Structure extinction colourmap (absolute linear scale).

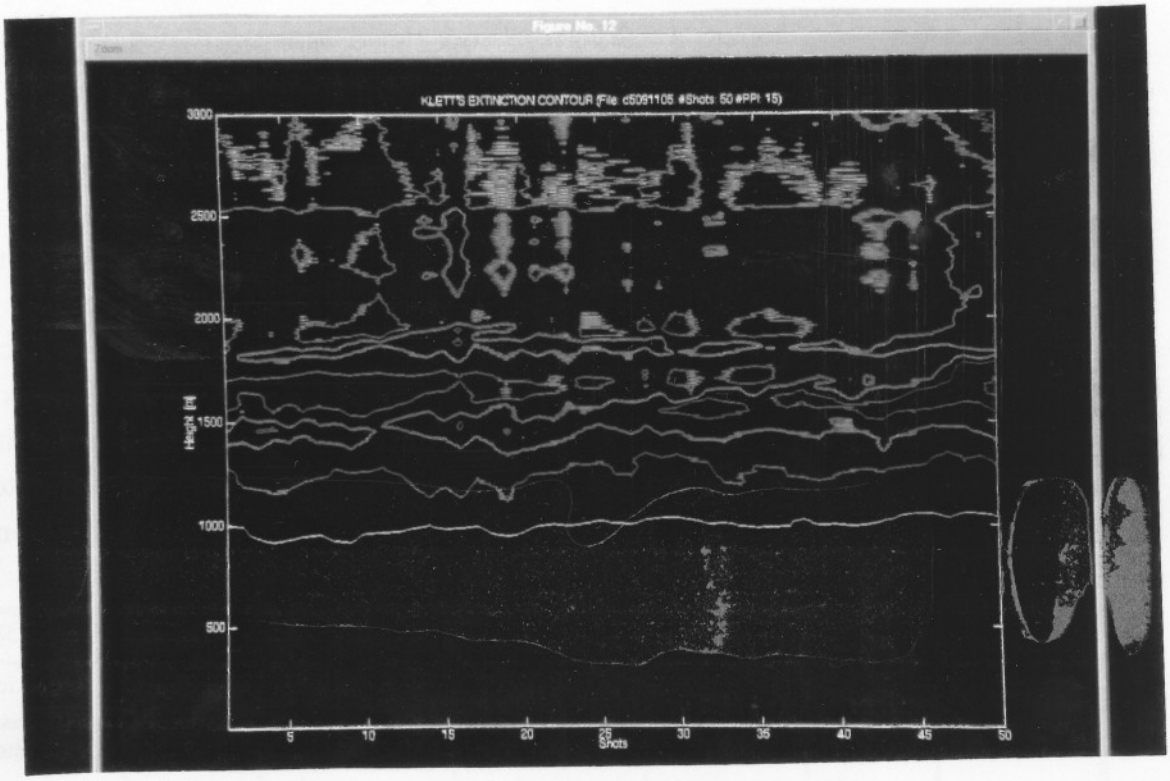

Fig. 46 Structure extinction contourmap (linear scale).

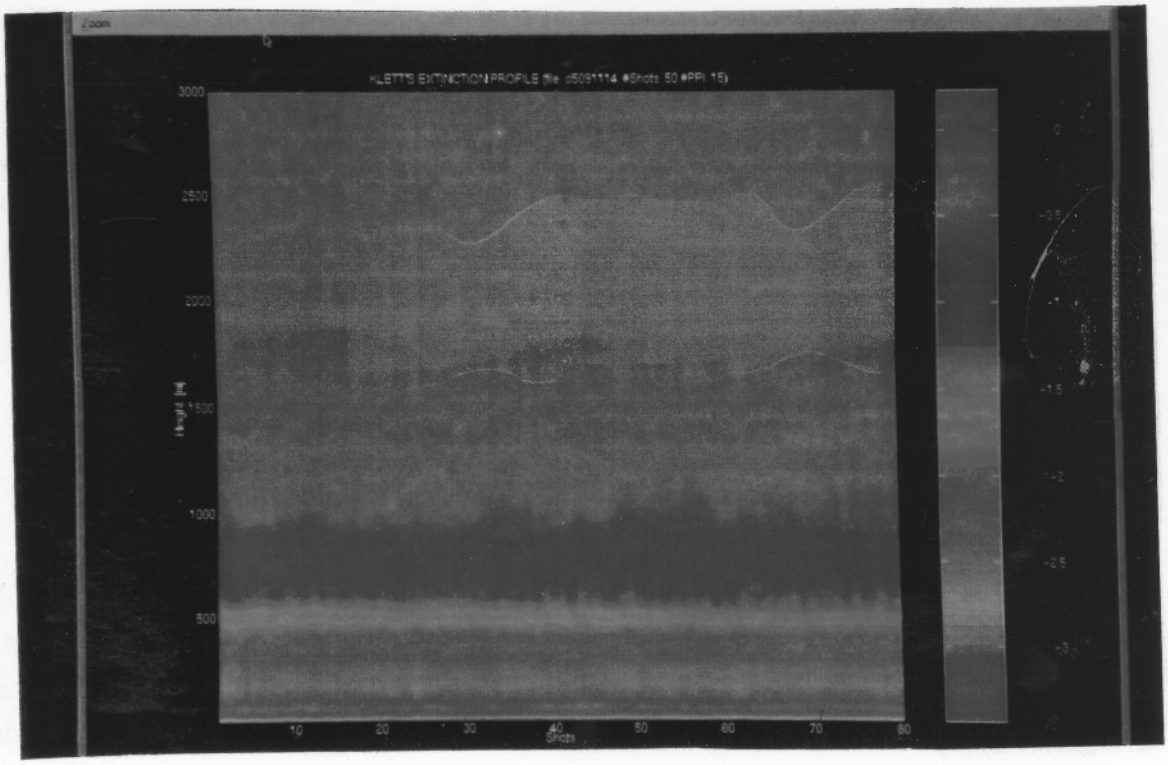

Fig.47 Structure extinction colourmap (absolute log scale).

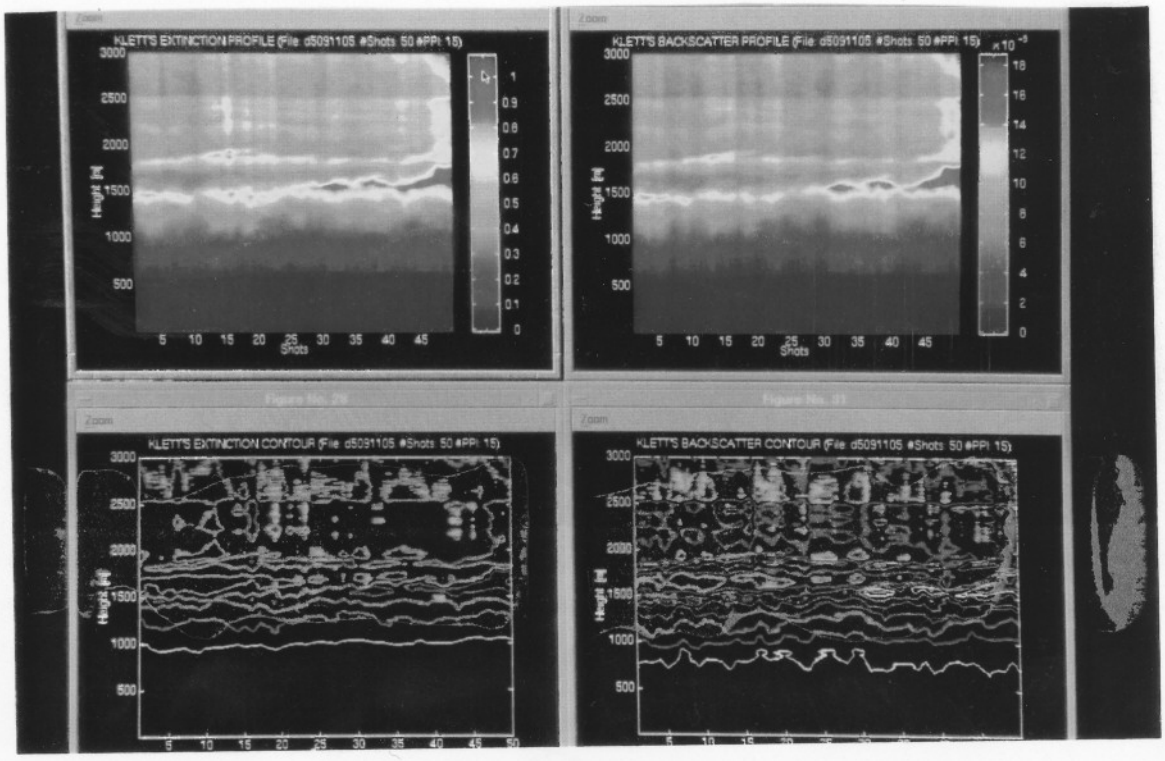

Fig.48 Structure extinction and backscatter profiles (absolute linear scale).

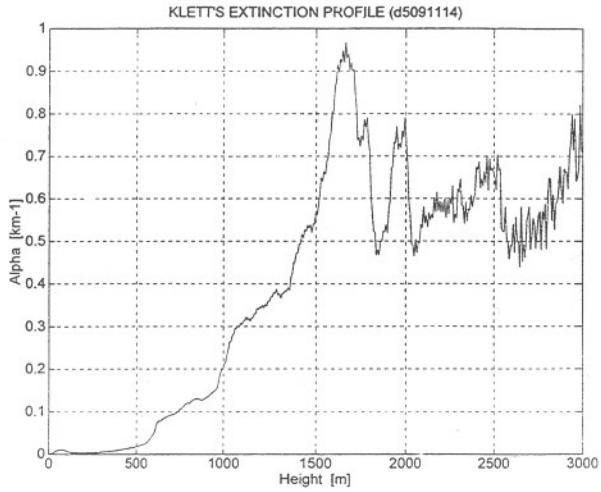

Fig.49 Structure extinction profile (Sept. 25th at 11:14 h).

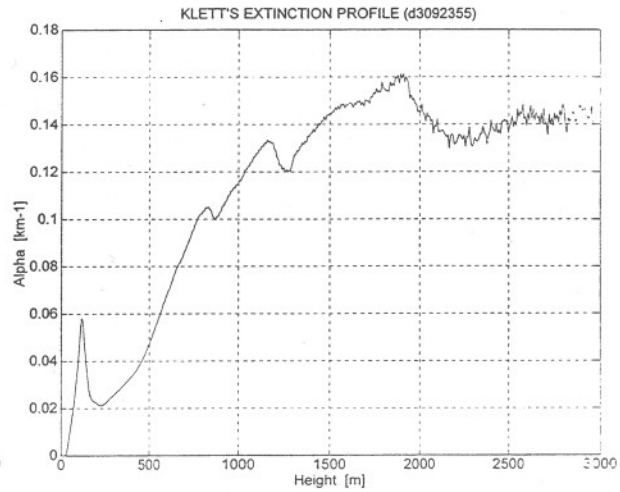

Fig.50 Structure extinction profile (Sept. 23rd at 23:55 h).

calibration at long range, R_{max}. To corroborate the extent of calibration error it would be very valuable the help of balloon-borne probes and other remote sensing equipment.

Errors due to over or underestimation of the correlation constant, k are easy to estimate since the shape of the profile is very sensitive to its value and even, for moderate errors, the profile can be seriously distorted. To guess a suitable value for k the procedure explained in Sect.2.1.2 is followed, either automatically of manually. This usually leads to overestimated errors below *10 %,* which represent around *2 % rms error* in the inversion of the extinction-profile.

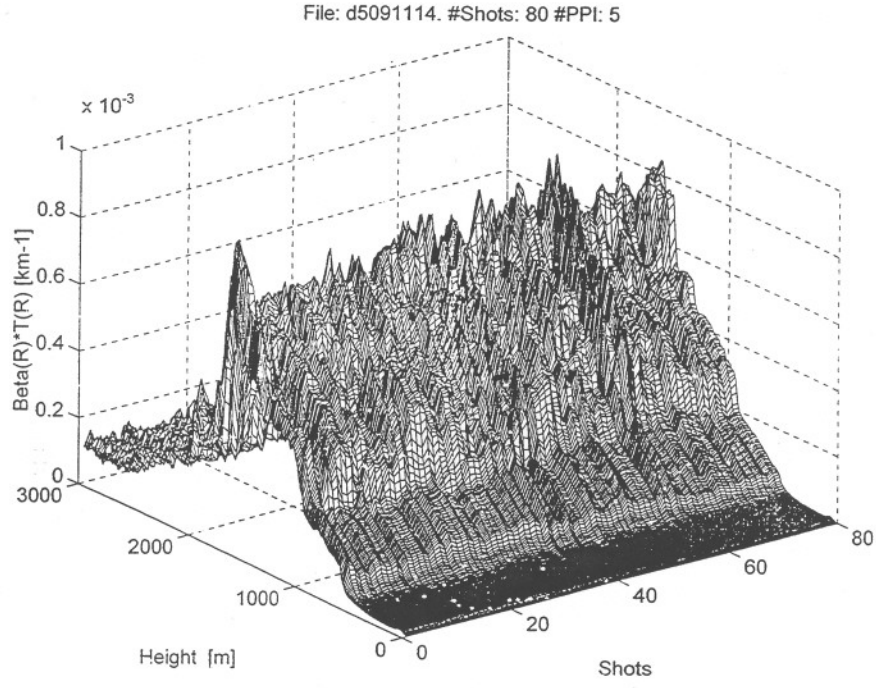

Fig.51 R^2-corrected signals vs. range and time.

4. CLOUD STUDIES

4.1 Ceilometry

The measurement of cloud base height or *ceiling* by lidar is very straightforward, particularly when the lower surface of the cloud is well defined [9]. In this case, the rapid increase of signal that marks the backscattered return form the cloud base can be readily distinguished and used to operated a timing counter, from which height can be read out in digital form. This has been used in commercial lidar *ceilometers*.

Since the critical factor in landing an aircraft is the height from which the pilot, looking along a slant path, can acquire visual reference, ceilometers are useful instrument in avionics. At the airport of Barcelona there is such an equipment.

The operation of the UPC lidar system designed as a ceilometer is shown by the plots of Fig.52, Fig.53 and Fig.54. These figures represent clouds around 6000-m height (possibly *cirrus* cloud) which were hardly seen by the eye, 3500-m height (possibly, *altostratus*) and 500-m height (low altitude storm clouds), respectively. For comparison purposes with subsequent sections, these plots represent cloud extinction (km^{-1}) versus height and time but for ceilometry studies it would have been enough with a simple R^2-*corrected* or, equivalently, β-*T product* presentation.

While commercial ceilometers do well with well defined cloud bases, their performance degrades on ragged or diffuse cloud bases, with patches of cloud below as in Fig.52, Fig.53 and Fig.54. Such condition are characteristic of much low cloud, especially when visibility at the surface is reduced by mist of fog that tend to merge with the cloud layer aloft. Quite often in stormy days, this phenomenon be seen in St.Pere Martir hill near the university campus (UPC, Campus Nord, Barcelona). It is clearly illustrated by Fig.54, where dynamism of different cloud layers is fairly evident.

From the same figures, it can be seen that the observations of clouds in general and the measurement of *layer thickness* and *cloud top height* (by difference to the ceilometers, which measure cloud bottom height) is also readily accomplished by the lidar this work has contributed to design and built and has obvious applications in meteorological research. Even the very tenuous cirrus clouds at *6000-m* height, nearly invisible to the eye, can readily be detected and their structure and shape mapped. Fig.56. Fig.58 and Fig.66 illustrate such structure for different types of clouds.

The observation of atmospheric motion is also possible from Fig.52, Fig.53 and Fig.54 but wind speed determination by tracking cloud signatures in the control monitor is impossible with the actual vertical configuration. Deriving air motion from successive observations of fortuitous inhomogeneities in *clear air* are being investigated.

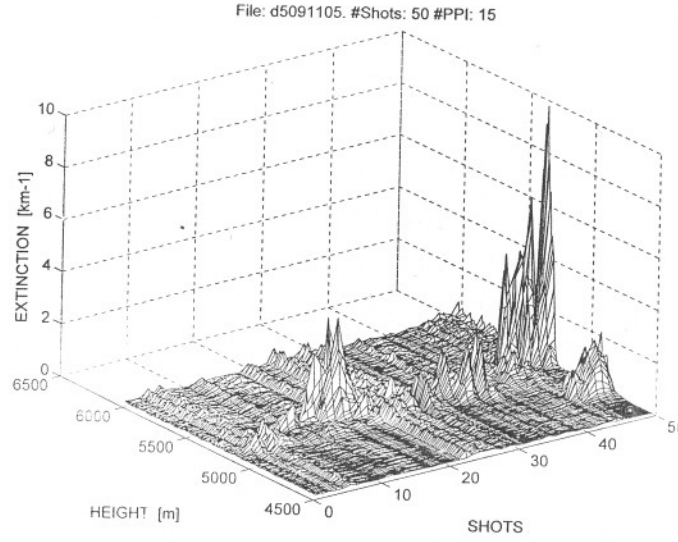

Fig.52 High clouds between 4500 and 6000 m.

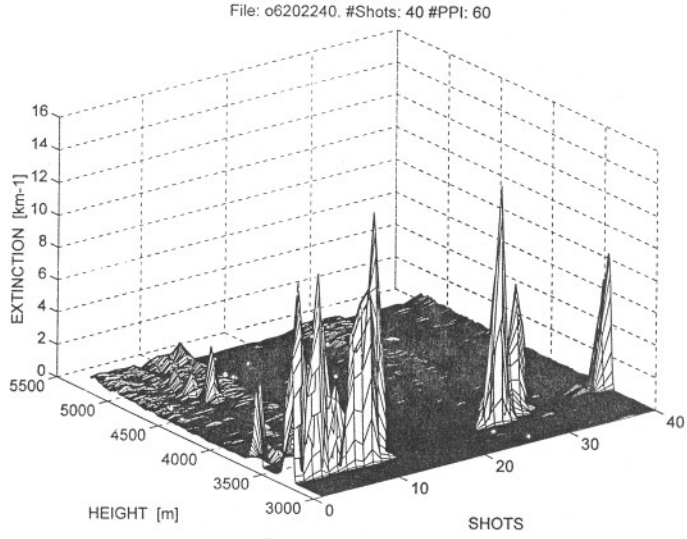

Fig.53 Medium height clouds around 3500-m.

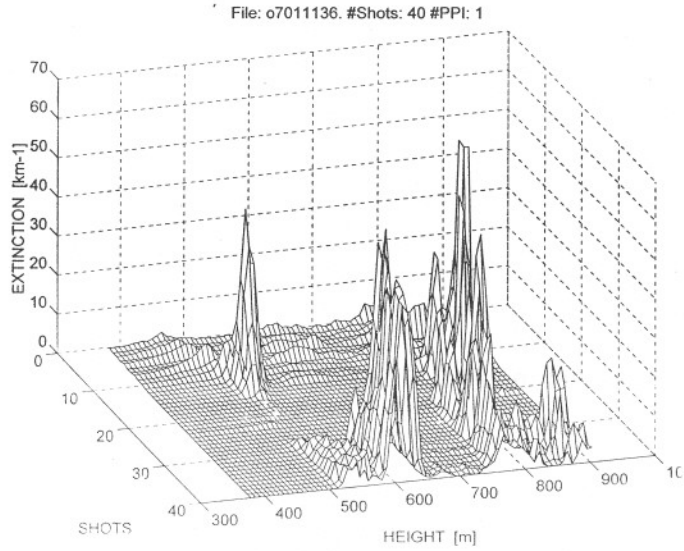

Fig.54 Storm clouds between 500 and 900 m.

Fig.55 Extinction into a cloud at 6-km height.

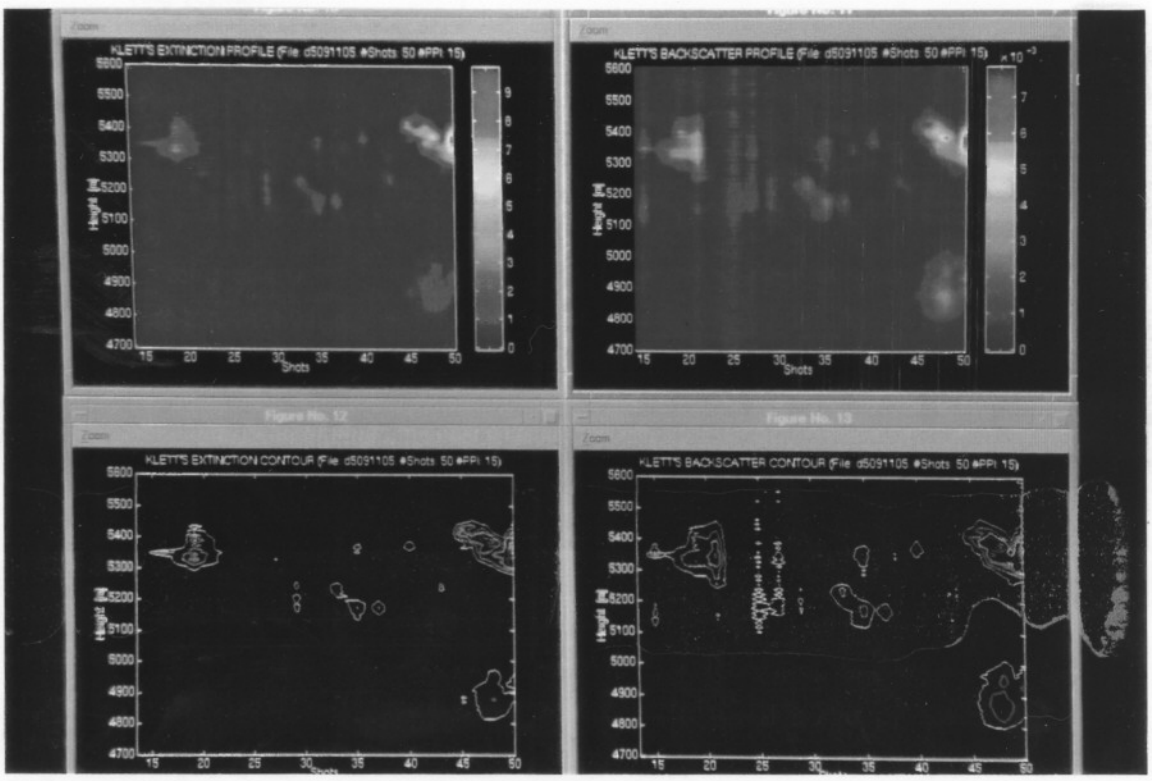

Fig.56 Extinction and backscatter maps for clouds at 6-km height.

4.2 Retrieval of the extinction profile

Following the same inversion procedures reported in Sect.3.2, Fig.59, Fig.60 and Fig.61 show Klett's extinction profiles for three different clouds into the mesh of Fig.52 (6000-m height cirrus clouds), Fig.62 for the altostratus clouds around 3500-m height and Fig.63 and Fig.64 for the storm clouds around 500-m height. Likewise, Tab.2 compares the inverted peak extinctions with reported values in the literature. In all cases, the results retrieved are in very close agreement apart from the expected mismatch in the backscatter-coefficient due to the optical overlap factor miscalibration. As discussed in Sect.3.2, extensive error analysis would involve correlation with alternative remote sensing instrumentation.

As for Tab.2, it must be cautioned that *the atmospheric condition reported refer to terminology used in Fig.5, Chap.8, Sect.1.3,* and, in this way, cirrus clouds are identified as thick hazes for they have similar extinctions.

A point worth mentioning here is that for the cloud studied the correlation constant k has taken values between *0.67-0.7* with the exception of low-extinction cirrus cloud wherein k has approached the unity values, as in the urban hazes which were described in Sect.3.2.

INVERSION				ATMOSPHERIC CONDITION based on refs.[9] [25]		
Possible type	**Height [m]**	**α_{inv} [km^{-1}]**	**β_{inv} [km^{-1}]**	**α_{typ} [km^{-1}]**	**β_{typ} [km^{-1}]**	**Condition**
Cirrus	4400-6000	1.5-7	$4.5\text{-}7\cdot10^{-3}$	1-4	$5\text{-}40\cdot10^{-2}$	thick haze
Altostratus	≈3500	≈7.5	$2\text{-}3\cdot10^{-3}$	10	$4\text{-}6\cdot10^{-1}$	light water cloud
Storm cloud	500-900	≈50	$\approx5\cdot10^{-3}$	10^{2}	4-6	dense water cloud

Tab.2 Comparison between structure optical parameters inverted and referenced.

The capability of lidar to observe cirrus inner structure reveals wave patterns of much interest in connection with meteorological studies. This cloud structure is often called *wave clouds* [9] (p.121). The amplitude and length of such standing waves are readily shown by the cross section patterns of the clouds. Fig.55, Fig.57 and in less detail, Fig.65 may well correspond to cross-sections of this type (extinction absolute value is shown).

Successive cross-sections enable to understand how the wave mechanism change as the wind flow and temperature conditions vary. Because of the low PRF of the Nd:YAG laser available, when these observations were made, the lidar cross-sections for these clouds take several minutes to observe. If higher data rates were possible, higher resolution in space an time would extend the technique to study dynamic features of the inner structure of a cloud or other significant atmospheric motions, though it is beyond the scope of this work.

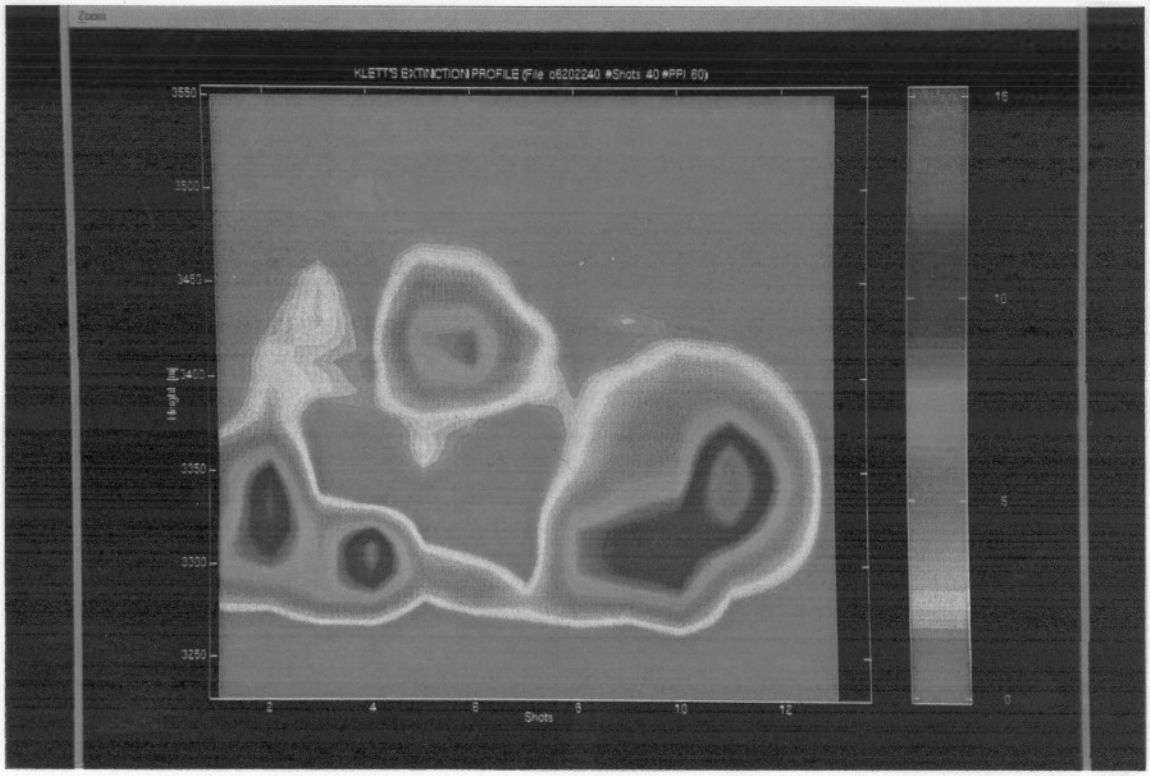

Fig.57 Extinction into a cloud at 3500-m height.

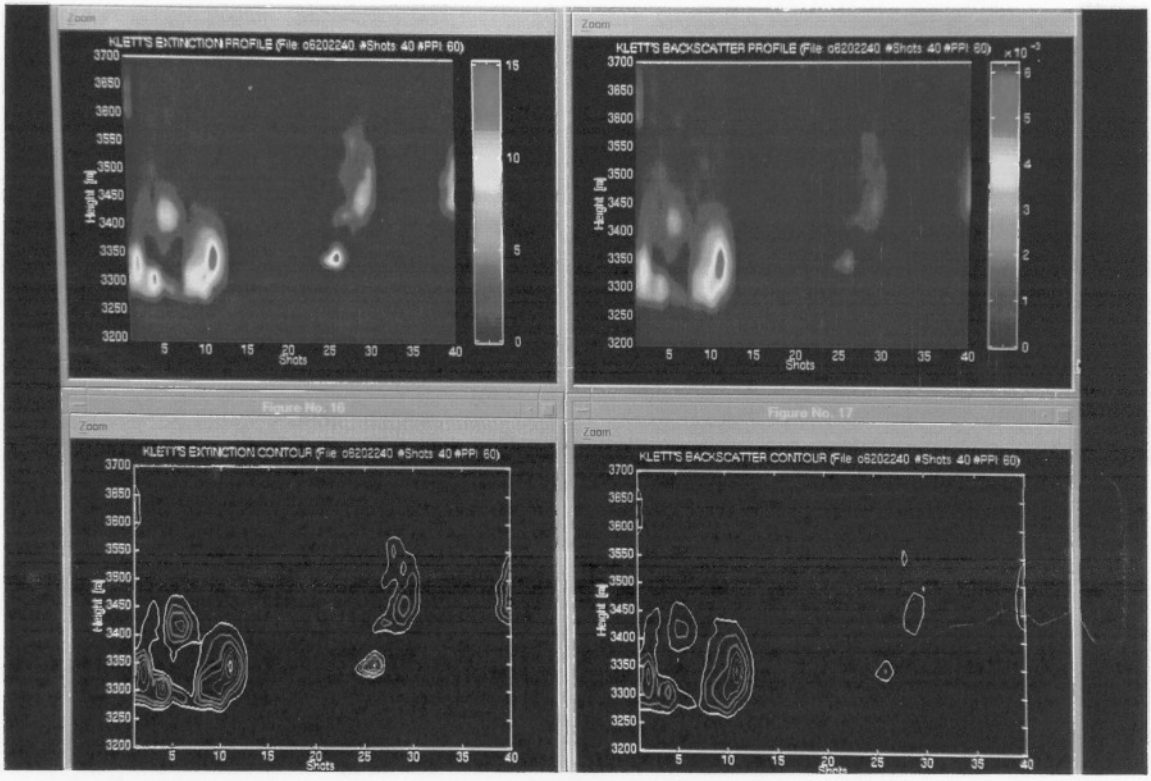

Fig.58 Extinction and backscatter maps for clouds at 3500-m height.

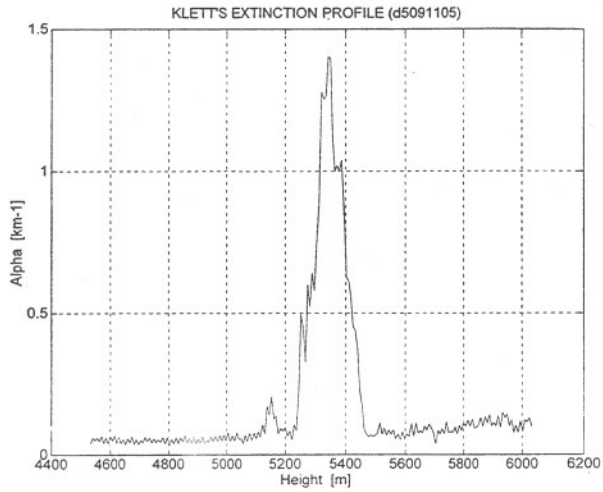

Fig.59 6-km height cloud extinction (I).

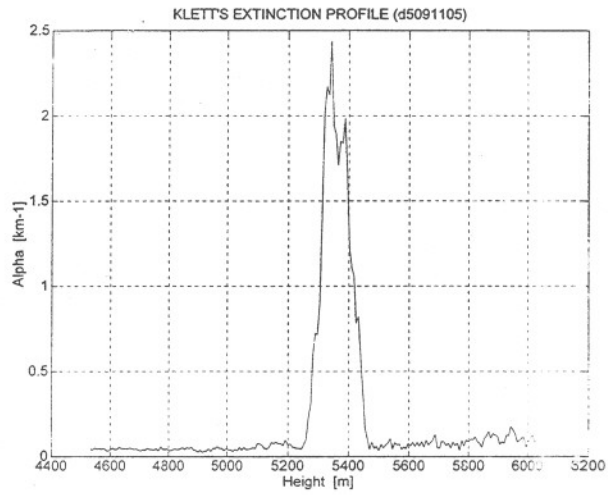

Fig.60 6-km height cloud extinction (II).

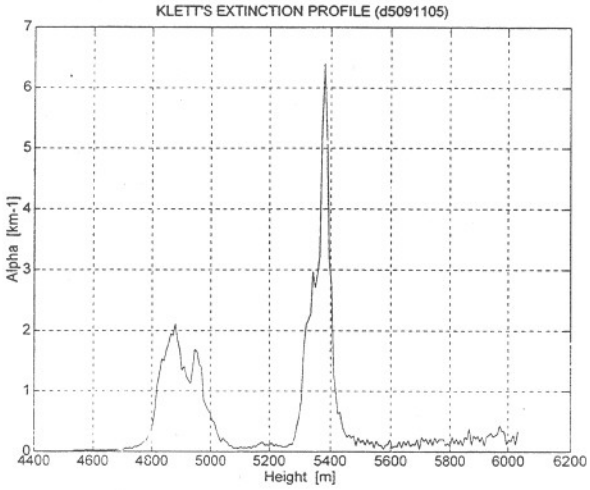

Fig.61 6-km height cloud extinction (III).

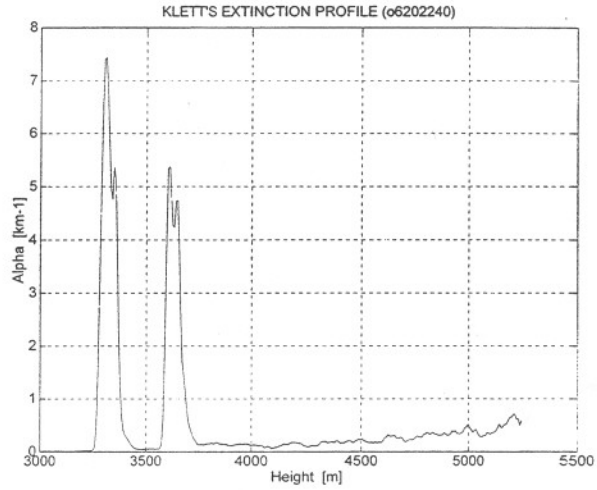

Fig.62 3.5-km height cloud extinction.

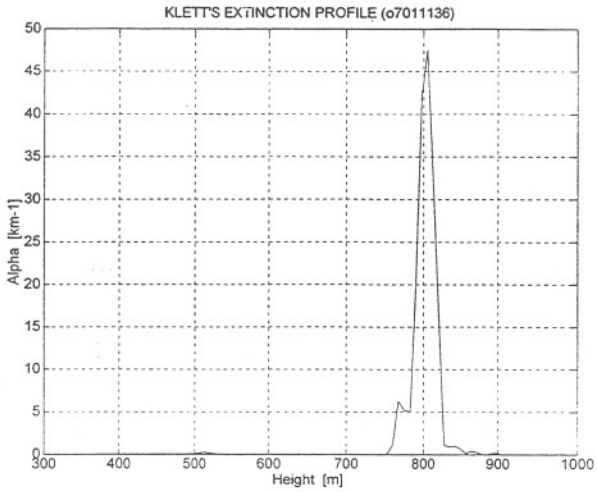

Fig.63 Storm cloud extinction (I).

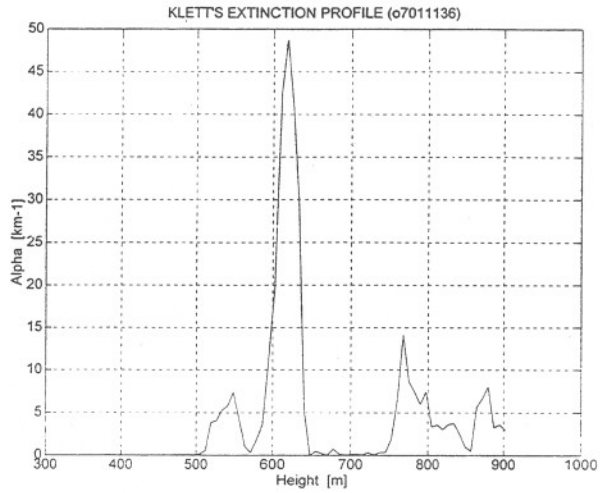

Fig.64 Storm cloud extinction (II).

NOTE: Extinction plots are show on fixed scale.

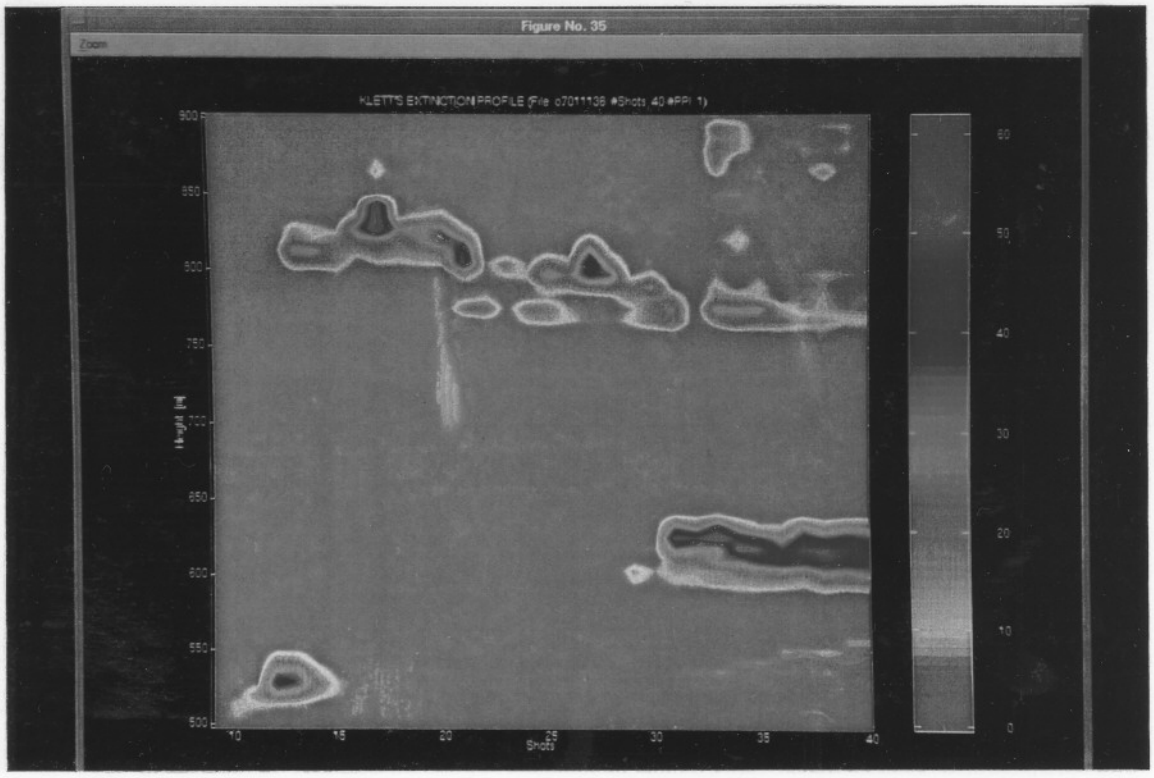

Fig.65 Extinction into a storm cloud at 500-m height.

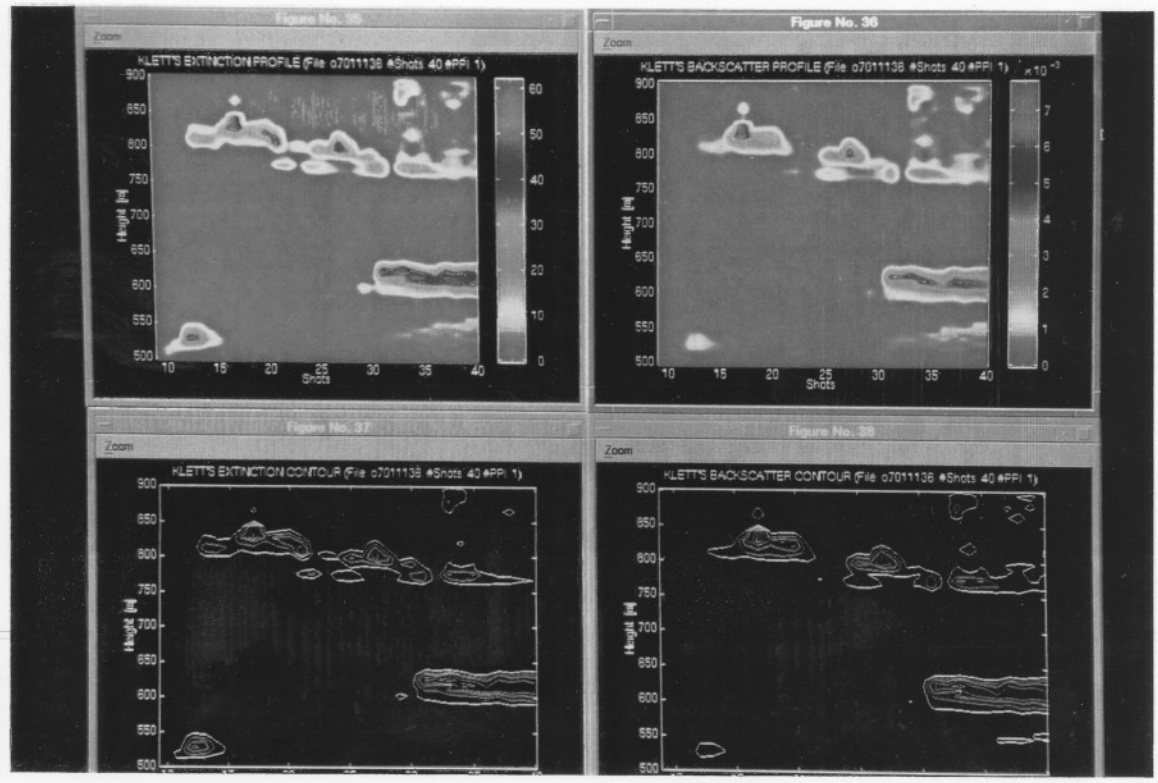

Fig.66 Extinction and backscatter maps for storm clouds.

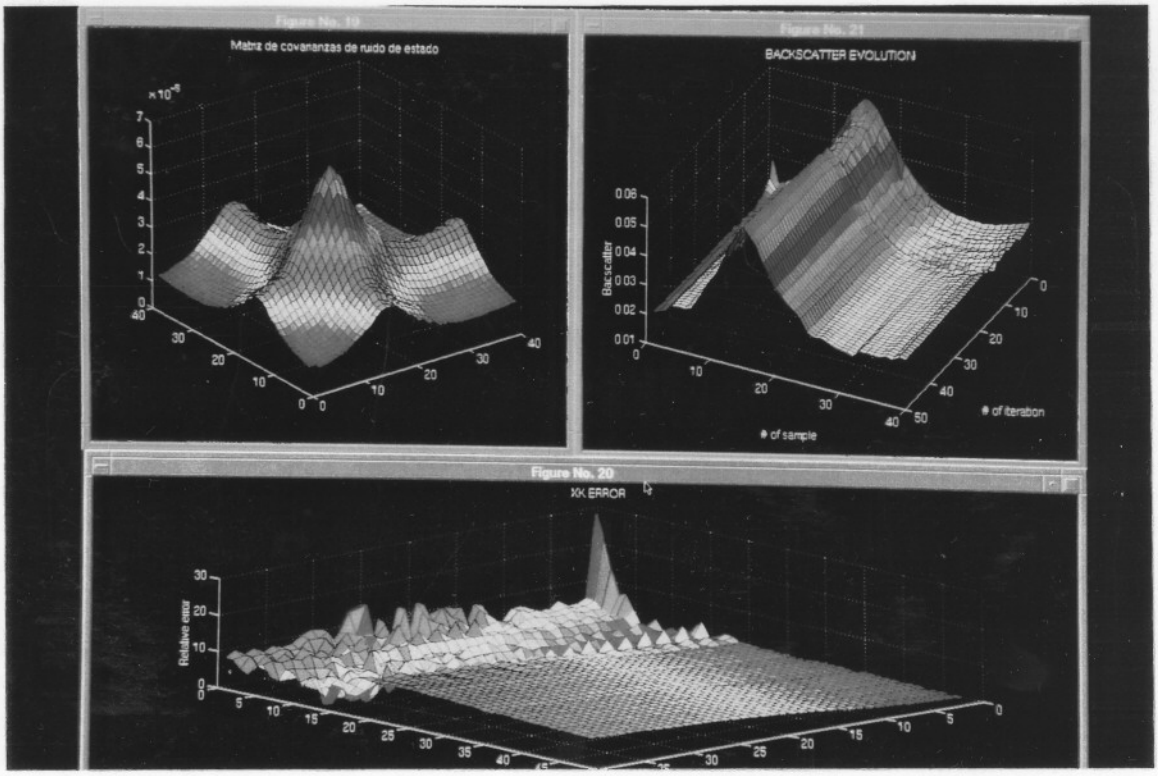

Fig.67 State-noise covariance matrix and Kalman filter evolution.

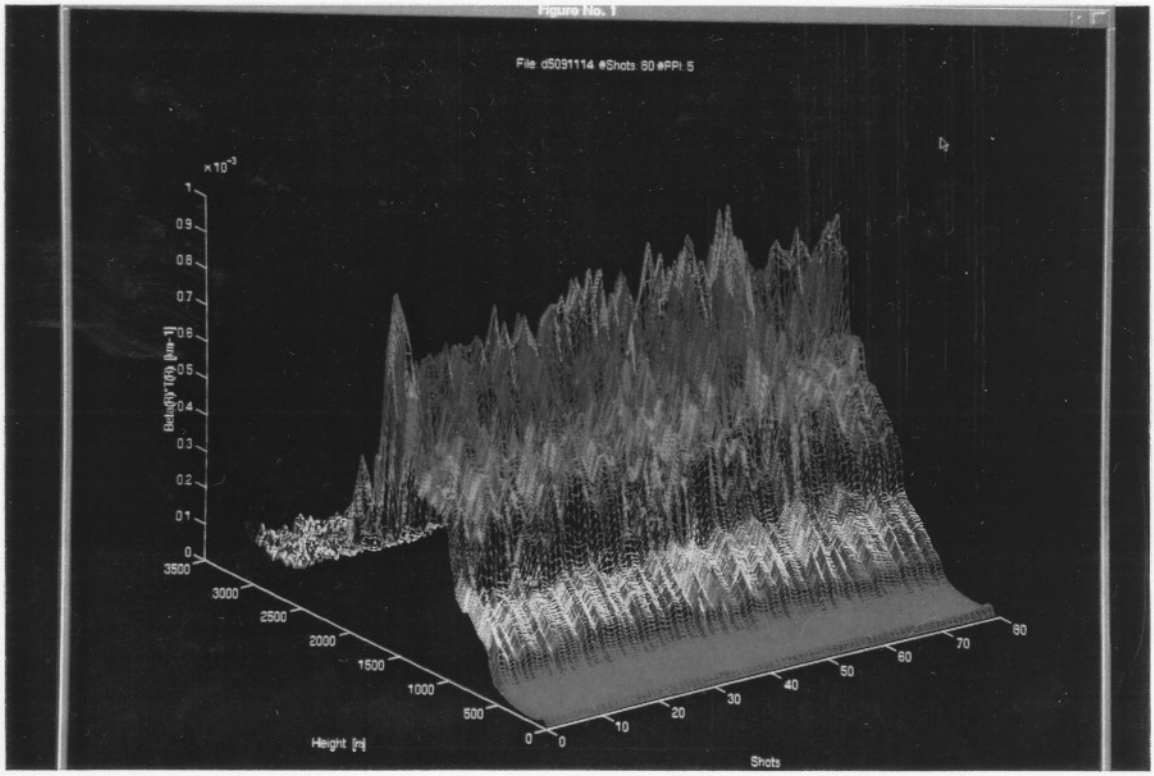

Fig.68 Live-scene observables for the Kalman filter array.